1   Sediment provenance changes in the western Arctic Ocean in response to ice-

2   rafting, sea-level and oceanic circulation variations since the last deglaciation

3   Charles-Edouard Deschamps [a,*], Jean-Carlos Montero-Serrano [a], Guillaume St-Onge [a],

4   [a] Institut des sciences de la mer de Rimouski, Canada Research Chair in Marine Geology, Université du Québec à

5   Rimouski & GEOTOP, 310 allée des Ursulines, Rimouski, Québec, G5L 2Z9, Canada

6   *Corresponding author: C-E. Deschamps. E-mail address: deschampscharlesedouard@gmail.com

7   **Key points**

8   1. Coupling grain-size, geochemical and mineralogical proxies in the Chukchi-Alaskan and

9   Canadian Beaufort margins.

10   2. Sediment unmixing model allows quantifying variations in sediment provenance and transport

11   in the western Arctic Ocean.

12   3. The dolomite-rich ice-rafted debris layers in both the Chukchi and Beaufort margins originate

13   from the Amundsen Gulf Ice Stream.

14   4. Quartz- and Zr-rich ice-rafted debris layers are linked to meltwater discharges from the Brooks

15   Range glacier.

16   5. Evidence of the Lake Agassiz outburst flood at the beginning of the Younger Dryas in the

17   Canadian Beaufort margin.

18

19

20

21

22

23

Abstract. Two sediment piston cores were recovered from the Chukchi-Alaskan (05JPC) and Canadian Beaufort (02PC) margins to investigate grain-size, elemental geochemical and mineralogical compositions. This allowed the reconstruction of changes in detrital sediment provenance and transport related to climate variability since the last deglaciation. The end-member modelling analyses of grain-size indicate that sea ice and nepheloid transport as well as the Mackenzie River sediment plume are major factors influencing sedimentation in the Chukchi-Alaskan and Canadian Beaufort margins, respectively. Unmixing of the sediment composition indicates that detrital sediments in core 02PC are derived mainly from the Mackenzie River, whereas sediments from core 05JPC are derived mainly from the Mackenzie River during the deglaciation and include a mixture of Holocene sediments from the Bering Strait inflow, Mackenzie River, and Eurasian margin. The dolomite-rich IRD recorded in both cores could be related to the different phases of iceberg discharges from the Amundsen Gulf Ice Stream. Quartz and feldspar-rich IRD dated at 13 and 10.6 ka cal BP are related to the Lake Agassiz outburst in core 02PC and meltwater discharge from the Brooks Range glaciers in core 05JPC. Our detrital proxies in core 02PC support the hypothesis that large meltwater and iceberg discharges from the Lake Agassiz outburst to the Arctic Ocean and Amundsen Gulf ice stream may have triggered the Younger Dryas. Finally, similar trends observed between the regional sea-level curves and our detrital proxy data suggest that the sea-level changes in the western Arctic Ocean have an important influence on the sediment dynamic during the early- to mid-Holocene.

Keywords: Bulk and clay mineralogy; elemental geochemistry; grain-size distribution; sediment provenance; Canadian Beaufort Sea; Chukchi Sea.

2

1 Introduction

Sedimentation in the Arctic Ocean and marginal seas has many peculiar characteristics related to the dominance of terrigenous input, which is derived mainly from the surrounding continents with different mineral assemblages and geochemical signatures (Fagel et al., 2014; Maccali et al., 2013; Vogt, 1997; Darby et al., 2011). This land-derived terrigenous material originated from a cold climate under conditions of minimal chemical weathering, and therefore consists of weakly altered detrital particles from the original source rocks. This allows correlation between the mineralogical and geochemical signatures preserved in the Arctic shelf sediments and the petrographic composition of the surrounding continents (Gamboa et al., 2017). Detrital sediments are delivered into the Arctic Ocean mainly as suspended particulate matter and bed loads from several large river systems including the Mackenzie, Yukon, Kolyma, Lena, Ob, and Yenisei Rivers (Wagner et al., 2011), as well as from coastal erosion (Gamboa et al., 2017). In shallow continental margins, suspended terrigenous particles are further dispersed by ocean currents and/or incorporated into the sea ice during formation and are then transported over long distances by the surface currents throughout the Arctic Ocean, finally settling far from their source of origin (Darby et al., 2012).

Under this framework, a number of studies have characterized and compiled the regional mineralogical and geochemical composition of the detrital sediments over the continental shelf from the Eurasian Basin (Schoster et al., 2000; Viscosi-Shirley et al., 2003; Vogt, 1997), Chukchi Sea-Bering Strait (Kobayashi et al., 2016; Stein et al., 2017), Chukchi-Alaskan margin (Darby et al., 2012; Naidu et al., 1982; Naidu & Mowatt, 1983; Ortiz et al., 2009; Yamamoto et al., 2017), Canadian Beaufort Shelf and Amundsen Gulf (Gamboa et al., 2017; Naidu et al., 1971). These

3

69 datasets allow characterizing the regional surface sediment patterns of the mineralogical and

70 geochemical composition related to the main sediment sources in the circum-Artic region. Once

71 this first crucial step has been achieved, it is possible to use the mineralogical and geochemical

72 signatures preserved in the Arctic Ocean sedimentary records to reconstruct and better interpret

73 the past variations in sediment inputs, as well as the transport pathways related to late Quaternary

74 climate and oceanographic changes. However, most of the bulk mineralogical records that have

75 been generated do not quantify the contribution of possible sediment sources in the western

76 Arctic Ocean, nor their long-term variability. On the other hand, the high sedimentation rates

77 observed in the postglacial sedimentary sequences from the continental margins of the Canadian

78 Beaufort (~10-60 cm.ka^{-1}; Deschamps et al., 2017) and Chukchi (~30-300 cm.ka^{-1}; Barletta et al.,

79 2008; Lisé-Pronovost et al., 2009) seas in Arctic Ocean offer records for reconstructing sediment

80 dynamics and past climate conditions at the centennial to millennial time scales.

81

82 In this regard, in the present study, grain-size, mineralogical and elemental geochemical analysis

83 of the bulk (<2 mm) and clay (<2 μm) sediment fractions were carried out on two sediment

84 piston cores recovered from the Chukchi-Alaskan (core HLY01-05JPC) and Canadian Beaufort

85 (core AMD0214-02PC) margins in order to (1) assess the contributions from specific sediment

86 sources (e.g., East Siberian Sea, Kara Sea, Northwest Alaska, Mackenzie River, Bering Strait

87 inflow, and Canadian Arctic Archipelago) and (2) provide new insights on potential relations

88 between ice-rafting, sea-level and oceanic circulation variations and sediment dynamics in the

89 western Arctic Ocean since the last deglaciation. Thus, our study differs from these earlier

90 publications in terms of methodological approach (quantitative mineralogy and multiproxy

91 study), inter-margin comparison (Chukchi-Alaskan *vs.* Canadian Beaufort margins), and

4

92   enhanced discrimination of circum-Arctic sediment sources. Therefore, this multiproxy record

93   provides an opportunity to reconstruct sediment dynamics within the western Arctic Ocean since

94   the deglaciation.

95   ## 2   Regional Setting

96   ### *2.1   Oceanic circulation*

97   The Arctic surface oceanic circulation is related to two main, wind-driven circulation systems,

98   which are the anticyclonic Beaufort Gyre (BG) in the western Arctic and the Transpolar Drift

99   (TPD; Darby & Bischof, 2004; Tremblay et al., 1997). At a regional level, these surface

100   circulation regimes are controlled mainly by changes in the phase of large-scale atmospheric

101   patterns, such as the Arctic Oscillation (AO; Darby & Bischof, 2004; Darby et al., 2012) and the

102   Pacific Decadal Oscillation (PDO; (Overland et al., 1999), which are both significant natural

103   patterns in global climate variability. On the other hand, the Chukchi shelf circulation is

104   controlled by an inflow of Pacific waters via the Bering Strait (referred to as the Bering Strait

105   inflow), the Siberian coastal current, and the Atlantic Intermediate Water affecting the northern

106   margin (Pickart, 2004; Weingartner et al., 2005). The Pacific inflow can be divided into 3 major

107   branches (Figure 1). The first branch turns westward around Herald Canyon. The third branch

108   flows into Barrow Canyon, whereas the second branch flows between the first and the third

109   branches (Weingartner et al., 2005). The Bering Strait inflows are controlled mainly by the

110   Aleutian Low strength and position at the interannual time scales (Yamamoto et al., 2017).

111   Indeed, periods of strengthening of the Aleutian Low pressure center, located over the eastern

112   North Pacific, induce an increase of the Bering Strait inflow into the Arctic Ocean (Danielson et

113   al., 2014). On the Canadian Beaufort shelf, the anticyclonic BG pushes both surface currents and

5

114 sea ice westward at the shelf break. Conversely, closer to shore around the 50-m isobath, the

115 Beaufort Undercurrent transports both Pacific and Atlantic waters eastward along the continental

116 margin and into the Amundsen Gulf (Forest et al., 2011).

117 *2.2   Surrounding geology*

118 Because the Arctic Ocean is a semi-enclosed basin, detrital sediment source regions for the Arctic

119 are limited to the surrounding terrains: the Canadian Arctic Archipelago, the Mackenzie delta

120 region, Northern Alaska, the Chukchi Sea with Pacific influences, the East Siberian Sea, the

121 Laptev Sea, the Kara Sea, the Barents Sea, and the Pan-African terrains of Northern Greenland

122 (Fagel et al., 2014). These circum-Arctic sources areas have variable geological ages and tectonic

123 settings, and are therefore characterized by different petrographic signatures. The Canadian

124 Arctic Archipelago and the Mackenzie Delta region are comprise shales and sandstones from

125 marine and non-marine sedimentary rocks (Harrison et al., 2011). In addition, Banks and Victoria

126 Islands are composed of shale and sandstones rich in dolomite clasts, as well as quartz and

127 feldspar grains (Bischof & Darby, 1999). As part of the North American margin, the Canadian

128 Shield is made of Archean plutonic and metamorphic rocks (Padgham & Fyson, 1992). Alaskan

129 terrains include Canadian–Alaskan Cordillera, Brooks Range, and part of the North American

130 platform containing mostly metamorphic, and clastic rocks (Hamilton, 1986). The Siberian

131 platform is composed by Precambrian and Cambrian limestones, Jurassic to Cretaceous

132 terrigenous sediments and Quaternary alluvial material (Harrison et al., 2011). The volcanic areas

133 can be separate in different zones: the intraplate Okhtosk-Chukotka composed by acidic to

134 intermediate rocks predominating in the west and intermediate to basic rocks in the east (Viscosi-

135 Shirley et al., 2003b), as well as Bering Sea Basalt Province, and the Permian and Triassic

136　volcanic rocks of Siberian traps, and the convergent margins of the Pacific Aleutian (Harrison et

137　al., 2011).

2.3　Sedimentation

139　On the Canadian Beaufort shelf, most of the surficial seabed sediments are predominantly

140　composed of Holocene marine olive-grey silts and clays (Gamboa et al., 2017). Surface

141　sediments from the Chukchi Sea are composed of bioturbated grey to clayey silts (Kobayashi et

142　al., 2016). Modern sedimentation in the Chukchi Sea is believed to be mainly derived from

143　northeastern Siberia, Bering Strait inflow (especially from the Yukon River) and Mackenzie

144　River, whereas, the Canadian Beaufort margin sediment originates primarily from the Mackenzie

145　River basin (Darby et al., 2011; Gamboa et al., 2017; Kobayashi et al., 2016). Smaller Alaskan

146　rivers have a more local impact, but may have been a more important sediment source at the early

147　stages of the last transgression (Hill & Driscoll, 2008). During deglaciation and the early

148　Holocene, sediment inputs to the Chukchi and Beaufort margins were presumably higher due to

149　the rising sea level associated with meltwater and iceberg discharge from the retreating of large

150　ice sheets (Deschamps et al., 2017). During the Holocene or interglacial, sediment redistribution

151　is strongly controlled by bottom current while during deglacial/glacial period sea ice and ice

152　rafted debris (IRD) strongly affected sediment dispersal and deposition (Darby et al., 2009).

153　Several IRD have been recorded in the sedimentation along the North American margin

154　associated with the calving of the Laurentide and Innuitian Ice Sheets (Darby & Zimmerman,

155　2008).

3 Materials and methods

3.1 Samples, sediment characteristics and chronology

The sediment core HLY0501-05JPC (hereafter referred to as core 05JPC; location: 72°51.618'N, 158°25.26'W) was recovered from the Chukchi-Alaskan margin on board the USCGC Healy as part of the 2005 Healy-Oden Trans-Arctic Expedition (Darby et al., 2005); Figure 1b).Physical properties of the sediment core 05JPC have been previously published in Barletta et al. (2008). Core AMD0214-02PC (hereafter referred to as core 02PC; location: 71°22.910'N, 133°34.040'W) was collected on the Canadian Beaufort margin on board the CCGS Amundsen during the 2014 ArcticNet expedition (Montero-Serrano et al., 2014); Figure 1b). The age model and physical properties of the sediment core 02PC have been described in Deschamps et al. (2017). Note that cores 05JPC and 02PC were raised from the continental slope at 415 m and 998 m depth, respectively, where sediment deposition was not interrupted by sea-level changes. The sediment core 02PC was sampled evenly every 10 cm in the Holocene and IRD intervals, as well as every 20 cm in the deglacial interval for a total of 42 samples. The sediment core 05JPC was sampled every 60 cm in the Holocene interval and every 30 cm for the remaining sections (corresponding to the deglacial interval) for a total of 30 samples.

The sediment cores 05JPC and 02PC present two distinct sedimentary units. According to Barletta et al. (2008), the upper unit in core 05JPC is composed of olive-gray mud, and the second unit is characterized by dark-gray mud with sandy layers and IRD. Core 02PC consists of homogeneous olive-brown to dark-gray for the upper unit, while the second unit consists of dark-gray with the presence of white clasts and was interpreted as IRD (Deschamps et al., 2017). The sedimentation rate for core 02PC was lower in the postglacial parts (10-20 cm.ka^{-1}) and higher in

8

179   the glacial parts (60-300 cm.ka^{-1}). Based on the physical properties and grain-size analyses, the

180   IRD layers were found in the glacial unit in both cores. The IRD were identified between 1350

181   (IRD1A) and 1600 (IRD1B) cm in core 05JPC (Barletta et al., 2008). Likewise, the IRD in core

182   02PC consists of white clasts found between 140 and 160 cm (IRD1A), 320 and 350 cm (IRD2A)

183   as well as 350 and 360 cm (IRD2B). These fine-grained IRDs are generally < 63 µm, poorly

184   sorted, have sharp contacts, and consist mainly of rock flour (dolomite- and quartz-rich). These

185   IRD are interpreted to reflect enhanced meltwater discharge and iceberg rafting from the

186   Laurentide Ice Sheet (Andrews, 2000; Deschamps et al., 2017; Polyak et al., 2007; Lakeman et

187   al., 2018).

188

189   The age model of core 05JPC was constructed using a linear interpolation between the ^{14}C ages

190   for the Holocene and deglacial sections (Barletta et al., 2008) and assuming a ΔR=460 as

191   suggested in Darby et al. (2009). The best ^{14}C-based age control covers the interval of 2–6.9 ka

192   cal BP in 05JPC. Ages below this dated interval were extrapolated and our interpretations thus

193   remain hypothetic. However, the very similar paleomagnetic secular variations between core

194   05JPC and other Arctic records (Barletta et al., 2008) suggest a valid age model around 8.5-9 ka

195   cal BP. Based on this age model, core 05JPC spans the last 11 ka cal BP and IRD1A-B were

196   dated at 9.5 and 10.6 ka cal BP, respectively. In the same way, the age model of core 02PC

197   published in Deschamps et al. (2017) was improved using the new ages from the nearby core

198   56PC presented in Lakeman et al (2018) and assuming a ΔR= 335±85 for the Holocene interval

199   and a ΔR= 1000 for the deglacial interval (Coulthard et al., 2010; Hanslik et al., 2010).

200   Contemporaneous IRD peaks have been identified in magnetic susceptibility curves and used in

201   order to transfer the age model of core 56PC to core 02PC (see supplementary material). Finally,

9

202   core 02PC spans the last 13.2 ka cal BP and the IRD1A and IRD2A-2B are dated to ~11, 12.8

203   and 13 ka cal BP, respectively (Figure SM1).

3.2   *Grain-size distribution and end-member modelling analysis*

205   Sediment grain-size analyses were performed on the detrital bulk sediment samples using a

206   Beckman Coulter LS13320 laser diffraction grain-size analyzer following the protocol in

207   Deschamps et al. (2017). The grain-size distribution and statistical parameters (e.g. mean and

208   sorting) were calculated using the moment methods from the GRADISTAT software (Blott &

209   Pye 2001). The end-member modelling algorithm (EMMA), developed by Weltje (1997) and

210   adapted by Dietze et al. (2012), was applied to the grain-size data in order to extract meaningful

211   end-member (EM) grain-size distributions and estimate their proportional contribution to the

212   sediments. A more detailed description of the EMMA method that we applied can be found in

213   Dietze et al. (2012). Overall, the grain-size loadings, mean grain size and end-member modelling

214   analyses were used to investigate the sedimentary transfer regime because the sediment grain-size

215   distribution (primarily driven by sedimentary processes) reflects transport conditions (Dietze et

216   al., 2012; Gamboa et al., 2017).

3.3   *Geochemical and mineralogical analysis*

218   Before geochemical and mineralogical analysis, the sediment samples were rinsed five times with

219   distilled water after the removal of the organic matter fraction with 10 mL of hydrogen peroxide

220   (30% H_2O_2). Next, an aliquot of this sediment sample was used as the bulk fraction (< 2 mm),

221   whereas another aliquot was used to separate the clay-sized fraction (< 2 μm). A centrifuge-based

222   Atterberg method was used according to Stoke's Law to separate the clay-sized fraction. The

223   required settling times were calculated using the software SediCalc (Krumm, 2006).

224   Subsequently, aliquots of the separated bulk and clay-sized samples were oven dried overnight at

225   approximately 60°C and then slightly homogenized with an agate mortar. These homogenized

226   sediment fractions were used for geochemical and mineralogical analysis.

227   *3.3.1   Bulk elemental concentration*

228   A total of 14 elements (Al, Si, K, Mg, Ca, Ti, Mn, Fe, P, Sr, V, Cr, Zn, and Zr) were analyzed on

229   both bulk and clay-sized fractions by energy dispersive X-ray fluorescence (EDXRF)

230   spectrometry using a PANalytical Epsilon 3-XL. Before EDXRF analysis, samples were treated

231   by borate fusion in an automated fusion furnace (CLAISSE® M4 Fluxer). The analytical

232   procedures were similar to Gamboa et al. (2017). Analytical accuracy and precision were found

233   to be better than 1–5% for major elements and 5–10% for the other elements, as checked against

234   an international standard (USGS SDC-1) and analysis of replicate samples.

235   *3.3.2   Quantitative bulk mineralogy*

236   Bulk mineral associations (< 2 mm) were studied by quantitative X-ray diffraction (qXRD)

237   following the method developed by Eberl (2003) and used in other Quaternary glacial marine

238   studies that address sediment mineralogy (Andrews et al., 2015; Andrews et al., 2016; Darby et

239   al., 2011; Stein et al., 2017). For this, ~1 g of each sample was spiked with 0.25 g of corundum

240   and then ground in a McCrone micronizing mill using 5 mL of ethanol to obtain a homogenous

241   powder. The slurry was oven dried overnight at approximately 60 °C and then slightly

242   homogenized with an agate mortar. Next, 0.5 mL of vertrel was added to the mixture to prevent

243   the possible agglomeration of finer particles. The powder sample is then sieved (<300 μm), back-

244   loaded into the holders and analyzed on a PANalytical X'Pert Powder diffractometer. Samples

245   were scanned from 5° to 65° two-theta in steps of 0.02° two-theta, with a counting time of 4

246   seconds per step. For the quantification of the major mineralogical components, sediment XRD

247   scans obtained were converted into mineral weight percent (wt. %) using the Excel macro

248 program ROCKJOCK v11 (Eberl, 2003). This program uses a full-pattern fitting method that

249 permits the quantification of whole-sediment mineralogy with a precision of ±3 wt % (Eberl,

250 2003). The calculated total mineral wt. % was normalized to a sum of 100%. We focused on 15

251 key minerals (quartz, K-feldspar, plagioclase, calcite, dolomite, amphibole, Fe-bearing,

252 amorphous silica, kaolinite, chlorite, illite, biotite, muscovite, smectite and vermiculite) that

253 represented more than 96% of the overall mineral concentration in the bulk sediment sample.

254 *3.3.3 Clay mineralogy*

255 In this paper, clay minerals were quantified in the bulk sediment fraction (< 2 mm) using the

256 Excel macro program RockJock. However, nearly all previous clay-mineral provenance studies in

257 the Arctic Ocean used oriented mounts of the < 2 μm sediment fraction to identify and semi-

258 quantify the clay-mineral abundance, notably illite, kaolinite, chlorite, and smectite (Naidu et al.,

259 1971; Naidu et al., 1982; Naidu & Mowatt, 1983). Therefore, in this study, the clay-size fraction

260 of all sediment samples was isolated and analyzed in this manner for comparison. Clay minerals

261 were thus studied using XRD following established protocols (Bout-Roumazeilles et al., 1999; El

262 Ouahabi et al., 2017). The separated clay-sized fraction (<2 μm) was concentrated by

263 centrifugation and oriented by wet smearing on glass slides. The analyses were run from 2.49° to

264 32.49° 2θ on a PANalytical X'Pert Powder diffractometer. Three X-ray diagrams were

265 performed, after the sample was air-dried, ethylene glycol vapor saturation was completed for 12

266 h, followed by heating at 490 °C for 2 h.. Semi-quantitative estimation of clay mineral

267 abundances (smectite, illite, chlorite, kaolinite, vermiculite and a chlorite/smectite mixed layer)

268 based on peak areas was performed using the MacDiff® 4.2.5 software (Petschick, 2000). Similar

269 to others Arctic clay mineral studies (Schoster et al., 2000; Wahsner et al., 1999), clay mineral

270 contents were calculated by using the weighting factors introduced by Biscaye (1965) and

12

271   calculated to a sum of 100%. The error on the reproducibility of measurements is estimated to be

272   5% for each clay mineral, as checked during the analysis of replicate samples. Overall, the

273   combinations of both RockJock and oriented mounted methods are supporting each other and

274   give independent information (e.g., Darby et al., 2011).

275   *3.3.4   Sediment unmixing model*

276   We used the non-linear unmixing Excel macro program SedUnMixMC (Andrews et al., 2015;

277   Andrews & Eberl, 2012; Andrews et al., 2016) to gain a quantitative understanding of the

278   downcore changes in bulk sediment provenance. To avoid misinterpretation of bulk

279   mineralogical results caused by the methodological differences between sources and downcore

280   sediment samples, all sediment source samples used here were processed for qXRD (Andrews et

281   al., 2016; Belt et al., 2010; Darby et al., 2011; Gamboa et al., 2017; Lakeman et al., 2018; Stein et

282   al., 2017; Table SM2).

283   *3.3.5   Statistical approach*

284   The mineralogical and geochemical data are of a compositional nature, that is, they are vectors of

285   non-negative values subjected to a constant-sum constraint (usually 100%). This implies that

286   relevant information is contained in the relative magnitudes, so mineralogical and geochemical

287   data analyses must focus on the ratios between components (Aitchison, 1990). Under this

288   framework, the vertical distributions of the sediment provenance proxies, as well as the

289   discriminant scatter plots based on mineralogical and geochemical data were represented here as

290   log-ratios. Note that a log-transformation will reduce the very high values and spread out the

291   small data values and is thus well suited for right-skewed distributions (Boogaart & Tolosana-

292   Delgado, 2013). Thus, compared to the raw data, the log-ratio scatter plots exhibit better

293   sediment discrimination. In addition, discriminant and membership's probability analyses were

13

294 performed using the mineralogical dataset with the goal of ascertaining whether the differences

295 observed between each sediment source area are statistically valid (Andrews & Vogt, 2014;

296 Figure 2a-b). Prior to discriminant and membership's probability analyses, a log-centered (clr)

297 transform was applied to the dataset (Aitchison, 1990). Both analyses were conducted with "R"

298 software using the packages "adegenet" (Jombart, 2008) and "compositions" (Boogaart &

299 Tolosana-Delgado, 2008).

300 All analytical data presented are available electronically in the PANGAEA database

301 (https://www.pangaea.de/).

302 ## 4   Results and interpretations

303 *4.1   Grain-size distribution and end-member modeling*

304 The algorithm of the end-member modelling analysis EMMA showed a polymodal distribution

305 and revealed a three-EM model in cores 05JPC and 02PC (Figure 3a). This explains more than

306 95% of the total variance. The end-member EM3 is associated with medium to coarse silts (10 to

307 30 µm), end-members EM2 correspond to fine to medium silts (2 to 10 µm), and end-member

308 EM1 is associated with clay to fine silts (0 to 4 µm). Finding the same grain-size end-members in

309 both margins highlights the robustness of the results, and suggests that both margins are probably

310 influenced by similar sedimentary processes. The relative contributions of these end-members are

311 plotted against depth in Figure 3b. Darby et al. (2009) have shown the detailed grain-size

312 distribution for sediment transport processes in the western Arctic Ocean using varimax-rotated

313 principal component analysis on several Holocene sediment cores in the Chukchi Sea and

314 including core 05JPC. In their study, they found four main end-members: (i) EM <0.5 µm relates

315 to suspension freezing and sediment wash load; (ii) EM centered on 2 µm relates to anchor sea

14

316 ice; (ii) EM centered on 5 μm is associated with the non-cohesive (sortable) fine silt that is

317 commonly transported in suspension by weak currents along the bottom or in nepheloid layers

318 above the bottom, and (iv) specific to the Chukchi margin, EM of 43-64 μm is associated with

319 intermittent suspended load. Overall, these grain size end member obtained by Darby et al.

320 (2009) are similar to then obtain in this study, and therefore, we infer that our grain-size pattern

321 reflects the same sedimentary processes. However, surface sediments derived from the

322 Mackenzie River are also characterized by a fine to medium grain-size (4-5 μm; Gamboa et al.,

323 2017), which is similar to the EM centered on 5 μm that is related to nepheloid transport (Darby

324 et al., 2009). Thus, this end-member could be interpreted differently between the Chukchi

325 (nepheloid transport) and Canadian Beaufort margins (Mackenzie River sediment plume). Based

326 on these results, the Log(EM1/EM2) ratio is used to elucidate downcore variations in the

327 proportion of grains transported by sea ice or nepheloid flow for core 05JPC and by sea ice

328 and/or Mackenzie River discharges for core 02PC.

329 *4.2   Elemental geochemistry*

330 Stratigraphic distributions of the elemental geochemical data from the two sedimentary cores

331 studied here are shown in Figure S2. Looking at the variation of the proportion between the

332 different fractions (bulk and clay), we can observe 2 groups with a different behavior. The first

333 group was related to elements with a higher concentration in the bulk fraction, which included Si,

334 Ti, and Zr, as well as Ca, Mg, and Mn in the IRD intervals. However, note that Ca and Mg in the

335 IRD layers are more enriched in core 02PC than in core 05JPC (maximum values of ~15 wt %

336 and ~3.5 wt %, respectively). The second group was linked to elements with a higher

337 concentration in the clay fraction, which included Al, K, Fe, V, and Zn for both cores. The

338 downcore variations are quite similar between the bulk and clay fractions in core 02PC.

15

339   However, some differences in the long-term variations between the bulk and clay fractions are

340   observed in core 05JPC with an increase of Ca, Mg and Fe in the clay fraction during the early to

341   late Holocene (Fig. S5).

342

343   Because Al and Si are associated to clay minerals, aluminosilicates and quartz, and Ca is

344   associated to carbonates, the ternary plot Al, Si, and Ca (expressed as oxides; Figure 4a) was used

345   in order to obtain a general geochemical classification of the sediments (Gamboa et al., 2017).

346   Sediments from cores 05JPC and 02PC are dominantly composed of detrital material, which is

347   similar to an average shale (Pourmand et al., 2012). However, sediments from core 02PC are

348   slightly enriched in Al and depleted in Si in both the bulk and clay fractions compared to core

349   05JPC. In addition, the clay fraction of core 02PC is also enriched in Al and K, whereas core

350   05JPC is enriched in Mg and Fe (Figure 4c). Likewise, bulk sediments from cores 02PC and

351   05JPC have a similar chemical composition to the sediments of the Mackenzie River and

352   Chukchi Shelf/Eurasian Rivers, respectively. In the bulk sediments, the IRD layers showed

353   higher Ca contents (dolomite) and plot along the mixing line from average shale to the detrital

354   carbonate end-member (Figure. 4a). These Ca-rich IRD layers have a similar composition to the

355   Canadian Arctic Archipelago sediments (including Banks and Victoria islands; (Belt et al., 2010;

356   Darby et al., 2011; Gamboa et al., 2017).

357

358   Based on all the results discussed above, we selected the Log(Ca/Al), Log(Mg/Al), Log(Zr/Al)

359   and Log(Fe/Al) ratios to reconstruct downcore changes in sediment provenance and transport on

360   the Chukchi-Alaskan and Canadian Beaufort margins since the last deglaciation (Figures 6-7).

361   Indeed, the grain-size changes could be investigated with Log(Zr/Al), because Zr is concentrated

362   in zircon grains in the coarser fraction and Al is preferentially associated with clay minerals and

16

363 aluminosilicates in the fine-grained fractions (von Eynatten et al., 2012). As discussed in Bischof

364 & Darby (1999) and Gamboa et al. (2017), sediments derive from the Canadian Shield, the

365 sedimentary platform along the Mackenzie Valley, and the Western Canadian Arctic Archipelago

366 are characterized by high contents (up to 2%) in iron-oxides, including hematite, goethite, pyrite,

367 maghemite and magnetite. Thus, high Log(Fe/Al) ratios could reflect a higher input of iron-

368 oxides entrained by icebergs from the Laurentide and Innuitian ice sheets (e.g., Bischof & Darby,

369 1999). In addition, a high Log(Ca/Al) and Log(Mg/Al) ratio may reflect a greater contribution

370 from detrital carbonates (such as, dolomite), whereas low ratios may suggest the input of

371 aluminosilicates (Gamboa et al., 2017).

372 *4.3 Bulk mineralogy*

373 Stratigraphic distributions of the bulk mineralogical data from the two sedimentary cores in this

374 study are shown in Figure S3. The mineralogy of the bulk sediment fraction from the Canadian

375 Beaufort and Chukchi-Alaskan margins is dominated by quartz (02JPC: 13–40%; 05JPC: 12-

376 39%), phyllosilicates, which includes kaolinite, chlorite, illite, biotite, muscovite, smectite and

377 vermiculite (02JPC: 47-80%; 05JPC: 30-50%), amorphous silica (02PC:0-4.5%; 05JPC:0-25%),

378 plagioclase (02JPC: 1-7%; 05JPC: 4-11%), K-feldspar (02JPC: 0-5%; 05JPC: 1-6%), dolomite

379 (02PC: up to 28%; 05JPC: up to 5%), and lower proportions (<1%) of Fe-bearing, amphibole and

380 pyroxene minerals. In general, quartz, phyllosilicates, plagioclase and K-feldspar represented

381 more than 80% of the overall mineral concentration in both sediment cores. However, K-feldspar,

382 plagioclase, muscovite, chlorite and vermiculite are more abundant in core 05JPC, whereas

383 quartz, illite and kaolinite are enriched in core 02PC (Figures 4c-d). In both sediment cores,

384 intervals with punctuated enrichments of dolomite (up to 28% for 02PC and up to 5% for 05JPC),

385 as well as in quartz (up to 40% in both cores) are observed in the IRD layers (Figure 5). Based on

17

386   these results, we performed a ternary plot of illite+kaolinite, total feldspars, and dolomite (Figure

387   4b) to obtain a general mineralogical discrimination of the potential source areas. The Bering

388   Strait and Eurasian sources are characterized by a higher total feldspar proportion, the sediments

389   from the Northern Alaska and Mackenzie River are related to higher illite+kaolinite contents, and

390   the sediments from the Banks and Victoria Island are enriched in dolomite. The sediments of core

391   02PC are mostly related to the Mackenzie River as potential sources, whereas the sediments of

392   core 05JPC seem to be composed by a mixture of sediments from the Eurasian margin, Bering

393   Strait and Mackenzie River. The sediments in the IRD layers present higher dolomite contents.

394   Overall, the relative abundance of dolomite, and the following ratios are used to trace sediment

395   provenance changes over time : Log[quartz/(K-feldspar+plagioclase)] or Log(Qz/Fsp),

396   Log[phylosillicates/(K-feldspar+plagioclase)] or Log(Phy/Fsp), and

397   Log(illite+kaolinite/chlorite+muscovite) or Log(I+K/C+Ms).

398   *4.4   Clay mineralogy*

399   Stratigraphic distributions of clay mineralogical data from the two sedimentary cores studied here

400   are shown in Figure S4. The clay mineral assemblage consists mainly of illite, kaolinite, chlorite

401   and vermiculite in both cores (Figure 5). Indeed, core 02JPC consists of illite (55-70%), kaolinite

402   (10-30%), chlorite (10-25%), vermiculite (0-20%) and a scarce abundance of a smectite/chlorite

403   mixed layer (0-8%, average, 1%) (Figure S4). The clay mineral assemblage for core 05JPC

404   consists of illite (30-70%), chlorite (10-20%), kaolinite (5-15%), vermiculite (5-55%) and

405   smectite/chlorite mixed layer (0-20%), which is present in much less abundance, with average

406   contents of 1% (Figure S4). Thus, as also shown in the bulk qXRD data, the major clay

407   mineralogical difference between the two sediment cores is the higher illite-kaolinite proportion

408   in core 02PC, whereas core 05JPC is relatively enriched in chlorite (See Supplementary

18

409   Material). These results are consistent with those reported for modern surface sediments on the

410   Chukchi Shelf and Beaufort Shelf (Kalinenko, 2001; Krylov et al., 2014; Naidu et al., 1982;

411   Naidu & Mowatt, 1983; Wahsner et al., 1999). Thus, we used the

412   Log(illite+kaolinite/chlorite+vermiculite) ratio or Log(I+K/C+V) to derive changes in transport

413   pathways (e.g., Bering Strait inflow) and the Log(illite/kaolinite) ratio or Log(I/K) to reconstruct

414   changes in sediment inputs within the Canadian Beaufort Shelf.

415   **5   Discussion**

416   Long-term changes in sediment sources were explored using the program SedUnMixMC

417   (Andrews & Eberl, 2012). As summarized in Asahara et al. (2012), modern sediment inputs in

418   the Chukchi Sea are mainly derived from northeastern Siberia and Bering Strait inflow, and

419   accessorily from the Mackenzie River. Based on this premise, we ran the SedUnMixMC on

420   sediment core 05JPC using the following sediment sources: Bering Strait, Northern Alaska,

421   Eastern Siberian-Laptev Seas, Mackenzie Trough-Canadian Beaufort Shelf and detrital

422   carbonates from the Canadian Arctic Archipelago, including the Banks/Victoria Islands (see

423   Supplementary Material). In core 02PC, we ran SedUnMixMC using surface samples from the

424   following sources: Mackenzie Trough-Canadian Beaufort Shelf, Canadian Arctic Archipelago,

425   Kara Sea and bed sands from the Mackenzie River basin (see Supplementary Material). The

426   boxplot based on principal component scores of geochemical and mineralogical data (See

427   Supplementary Material), ternary plot illite+kaolinite−total feldspars−dolomite (Figure 4b), the

428   Log(Qz/Fsp)−Log(I+K/C+Ms) crossplots (Figure 4d), as well as the discriminant and

429   membership probability analyses based on log ratio mineral data (Figure 2), indicate that these

19

430   potential source regions have mineral and chemical compositions that allow a reasonable degree

431   of sediment discrimination as indicated by their relatively high membership value (up to 90%).

432

433   In this context, the long-term variations observed in our mineralogical and geochemical records

434   are discussed below in terms of glacial and postglacial changes in detrital sediment supply,

435   provenance and transport and their possible relations with both the deglacial/Holocene climate

436   variability and relative sea-level variations.

437   *5.1   Deglacial/Holocene sediment dynamics (14 to 10.5 ka cal BP)*

438   *5.1.1   Canadian Beaufort Sea*

439   SedUnMixMC modelling indicated that the fine-grained feldspar, quartz and Zr-rich layer in core

440   02PC (IRD2B) dated at ~13 ka cal BP is mainly derived from the Mackenzie River (40 %, Figure

441   6h). Optically stimulated luminescence ages from the Mackenzie drainage basin suggest a major

442   routing of deglacial meltwaters from Lake Agassiz into the Arctic Ocean at 13±0.2 ka cal BP,

443   near the onset of the Younger Dryas (Murton et al., 2010). This observation concurred to

444   highlight that the quartz and feldspars-rich layers observed at ~13 ka cal BP in the Canadian

445   Beaufort margin may be related to an outburst flood from Lake Agassiz. We hypothesize that

446   meltwaters from the Lake Agassiz remobilized rock flour deposits that are characterized by an

447   abundance of quartz and feldspars from the northwest part of the Mackenzie River watershed

448   (Figure 8). Furthermore, SedUnMixMC modelling also indicated that dolomite-rich (Ca-Mg)

449   IRD layers (IRD1A and IRD2A) dated at 11 and 12.8 ka cal BP were originated from the

450   Canadian Arctic Archipelago (Figures 6h). Similar dolomite-rich IRD have been found on the

451   Lomonosov Ridge and in Fram Strait during the Younger Dryas chronozone (Hillaire-Marcel et

452   al., 2013; Maccali et al., 2013; Not & Hillaire-Marcel, 2012). Major purge from the M'Clure and

20

453   Amundsen Gulf ice stream was previously suggested by isotope data (Hillaire-Marcel et al.,

454   2013; Maccali et al., 2013), paleogeography study (Stokes et al., 2009) and numerical model

455   (Tarasov & Peltier, 2005) between 13 and 12.7 ka cal BP and may have played a role in the

456   slowdown of the Atlantic Meridional overturning circulation at the onset of the Younger Drays

457   (Condron & Winsor, 2012). Overall, our results support the hypothesis that large meltwater and

458   iceberg discharges from the Lake Agassiz outburst and Amundsen Gulf ice stream were more

459   likely to have triggered the Younger Dryas cooling by inhibited deep water formation in the

460   subpolar North Atlantic and weakened the strength of the Atlantic Meridional Overturning

461   Circulation (Condron & Winsor, 2012; Hillaire-Marcel et al., 2013; Lakeman et al., 2018;

462   Maccali et al., 2013; Not & Hillaire-Marcel, 2012; Tarasov & Peltier, 2005).

463

464   In core 02PC, the high quartz/total feldspars and phyllosilicates/total feldspars ratios observed

465   during the Younger Dryas interval suggest that the detrital sediments mainly originated from the

466   northern tributaries of the Mackenzie River (Figures 6,8A). Wickert (2016) suggested that

467   meltwater inputs to the Mackenzie River ended no later than 11 ka cal BP, when its eastern

468   tributaries were temporarily rerouted eastward due to a combination of ice retreat and glacial

469   isostatic depression. The age of 11 ka cal BP coincides with the decrease of the sedimentation

470   rates from 50 cm.ka^{-1} to 2 cm.ka^{-1} (Figure SM1). In addition, the low foraminifera abundance and

471   high terrestrial organic matter content observed in the nearby core 750PC (Scott et al., 2009) also

472   suggest higher Mackenzie River discharge to the Canadian Beaufort margin during this time,

473   providing support to our interpretations. Finally, in agreement with Stokes et al. (2005; 2006;

474   2009) and Dyke & Savelle (2000), we suggest that the IRD1A layers dated at 11 ka cal BP may

475   be linked to a retreat phase of the Amundsen Gulf Ice Stream occurring during the Meltwater

476   pulse 1B (Figure 8b).

477 *5.1.2   Chukchi-Alaskan margin*

478 The overall mineralogical and geochemical signatures characterizing core 05JPC around 11 ka

479 cal BP point to a detrital input from the Bering Strait and Eurasian margin (~30% each; Figure

480 6g). However, the increase of vermiculite and mixed-layer chlorite/smectite recorded in the clay

481 fraction in this interval together with lower Log(EM1/EM2) ratio suggest that most of the

482 sediments are mainly derived from the Bering Strait and redistributed by bottom (nepheloid)

483 currents to the shelf and continental slope (Figures 9-S5). In addition, amorphous silica

484 concentrations, derived from qXRD analysis also depict a sharp increase (up to 25%) in the same

485 interval (Figure 9). High amorphous silica concentrations in the Chukchi Sea sediments are

486 interpreted to represent times when biosilica-rich Pacific waters flowed through the Bering Strait

487 (Jakobsson et al., 2017). Indeed, the presence of amorphous silica, including diatoms,

488 radiolarians, siliceous sponges and silicoflagellates, is a characteristic signature of Pacific waters

489 today, and therefore, this proxy may also be used to track Pacific waters inflow in the western

490 Arctic Ocean (Jakobsson et al., 2017; Stein et al., 2017). Thus,we hypothesize that sediments in

491 this interval may be related to the initial opening of the Bering Strait at ~ 11 ka cal BP (Jakobsson

492 et al., 2017).

493

494 SedUnMixMC results from core 05JPC suggest that the fine-grained quartz and Zr-rich IRD

495 layers and dolomite-rich (Ca-Mg) IRD layers originate from the Northwest Alaska and the

496 Canadian Arctic Archipelago, respectively (Figure 7h). The quartz and Zr-rich, but carbonate-

497 poor sediment record at ~10.6 ka cal BP (IRD1B) is more consistent with a northwestern Alaskan

498 source (Polyak et al., 2007). Indeed, high-resolution seismic reflection data in conjunction with

499 sedimentological data from piston cores from the outer Chukchi margin are evidence of the

500 occurrence of meltwater discharges from the Brooks Range to the shelf occurring between 10 and

22

501   13 ka cal BP (Hill & Driscoll, 2008; 2010). At the opposite, the carbonate rich layers dated at 9.5

502   ka cal BP is more consistent with the Canadian Archipelago source. We infer that the dolomite-

503   rich IRD (IRD1A) layer at 9.5 ka cal BP may be related to the final retreat phase of the

504   Amundsen Gulf Ice Stream which ceased operating by ~9.5 ka cal BP (Stokes et al., 2009).

505   However, this carbonate rich layer is missing in the Canadian Beaufort margin, as such layer was

506   not identified in core 02PC at this time (Figure 6). A plausible explanation for this could be the

507   presence of a hiatus in the early to middle Holocene transition (Figure SM1B). This observation

508   is supported by the fact that sedimentation rates in core 02PC show a distinct decrease from 50

509   cm.ka^{-1} to 2 cm.ka^{-1} between 6 and 11 ka cal BP, which appears very large and abrupt. However,

510   the accumulation is thought to have been continuous because of the lack of sharp lithological

511   changes or sedimentological indicators of hiatus or mass flow transport in this part of the core

512   (Deschamps et al., 2017). In addition, this abrupt decrease in sedimentation rates is consistent

513   with major reduction of meltwater flow derived from the Mackenzie River (Wickert, 2016).

514   Alternatively, as ages after 8.5-9 ka cal BP in core 05JPC were extrapolated, and the IRD1A in

515   cores 05JPC and 02PC show similar mineralogical and geochemical signatures which are

516   consistent with a common source area (Figure 4). We thus hypothesize that the dolomite-rich

517   IRD1A in core 05JPC could be dated at 11 ka cal BP similar to IRD1A from core 02PC (Figure

518   SM1A). This IRD correlation would imply that the age for the opening of the Bering Strait may

519   be older than 11 ka cal BP (Jakobsson et al., 2017) as previously suggested by Keigwin et al.

520   (2006), England & Furze (2008) and Elias et al. (1992). Further investigations are required to

521   gain a more precise chronology of the age constraint for the Bering Land Bridge flooding.

23

5.2 Holocene sediment dynamics (10.5 ka cal BP to present)

5.2.1 Canadian Beaufort Sea

In the Canadian Beaufort margin, the Log(EM1/EM2) ratio from the core 02PC showed few variations from 10 ka cal BP to present, supporting the idea that stable sedimentation dynamics dominates throughout the Holocene (Figure 8b). Likewise, the sediment unmixing model suggests that Holocene detrital sediments are derived primarily from the Mackenzie River (>80%; Figures 7h-10). However, the slight changes observed in bulk and clay mineralogical signatures during the mid-Holocene relative to the deglacial interval (i.e., relatively enriched in total feldspars and illite; Figure 8b) may reflect changes in sediment provenance within the Mackenzie River basin. Indeed, the watershed lithology of the main Mackenzie River tributaries is composed of a mixture between shale and igneous rocks having granodioritic to granitic compositions (Dellinger et al., 2017; Millot et al., 2003). More specifically, the northern tributaries of the Mackenzie River (such as the Peel and Red Rivers) drain almost exclusively weathered marine sedimentary rocks (e.g., Cambrian to Cretaceous limestones and shales), which are enriched in phyllosilicates, quartz, and detrital carbonates, whereas granitic source rocks outcropping in the North American Cordillera (including the Rocky and the Mackenzie Mountains) and Canadian Shield are drained by the southern tributaries (such as the Liard and Slave Rivers), which are characterized by an abundance of total feldspars (Gamboa, 2017); Figure 8a). All these observations suggest that the proportion of sediments derived from the southern tributaries increased during the mid-Holocene. Thus, we hypothesized that the final recession of the LIS in the Mackenzie Valley after ~11-10.5 ka cal BP (Dyke, 2004) promoted a major remobilization of glaciogenic sediments derived from crystalline rocks as the Mackenzie River adjusted to the postglacial hydrologic regime. Alternatively, we cannot rule out the

24

545   possibility that Holocene changes in relative sea level could also influence sedimentation in the

546   Canadian Beaufort margin (Figure 8b). The sea level rise resulted in coastal retreat and likely

547   exerted significant control on the sedimentation on the Mackenzie Shelf during the early- to mid-

548   Holocene (Héquette et al., 1995). A minor proportion of fine silt detrital sediments in core 02PC

549   during the mid-Holocene may therefore also been supplied from sea level rise-induced coastal

550   erosion of fine-grained Pleistocene quartz- and feldspar-rich glacial tills outcropping along the

551   Tuktoyaktuk Peninsula (Gamboa et al., 2017; Vogt, 1997; Figure 8b). However, sediments from

552   the southern Mackenzie River tributaries and Tuktoyaktuk Peninsula are both characterized by

553   similar mineralogical signatures (Gamboa, 2017), and therefore, we cannot estimate the

554   proportion of sediment derived from coastal erosion. Additional information could be gained by

555   consideration of other provenance indicators such as radiogenic isotopes (Fagel et al., 2014).

556

557   *5.2.2   Chukchi-Alaskan margin*

558   SedUnMixMC modelling and the mineralogical ratios Log(I+K/C+V) and Log(Qz/Fsp) from

559   core 05JPC indicate that during the early Holocene (10.5–8 ka cal BP), the predominant sediment

560   source on the Chukchi-Alaskan margin was from the Mackenzie River (up to 92%). In addition,

561   Log(EM1/EM2) ratios revealed the dominance of clay- to fine silts-size particles during the early

562   Holocene, suggesting that sediment transport by sea ice predominates at this time (Figures 7h-

563   9b). In accordance with previous sedimentological studies (Darby et al., 2012; Not & Hillaire-

564   Marcel, 2012; Yamamoto et al., 2017), we hypothesize that sediment-laden meltwater plumes

565   derived from glacial erosion on the Mackenzie River basin were incorporated on the shelf by sea

566   ice. Sea ice was thus transported westwards along the Chukchi-Alaskan margin by an enhanced

567   BG during the early Holocene (Figure 10). Note that the BG strengthening during the early

25

568   Holocene is likely driven by a maximum boreal summer insolation (Gajewski, 2015; Yamamoto

569   et al., 2017).

570

571   During the Holocene, the Log(EM1/EM2) ratio reached minimum values between 8 and 6 ka cal

572   BP, suggesting that sediment transport during the mid-Holocene was dominated by bottom

573   currents (Figure 9b). In addition, the end-member EM3 (10 to 30 µm) records from both margins

574   during the deglacial interval are clearly associated with the IRD events (Figure 3b). However,

575   this end-member is still present during the Holocene interval for cores located in the Chukchi-

576   Alaskan margin (01JPC and 05JPC), while it did not influence the Holocene sedimentation in the

577   Canadian Beaufort shelf (Figure 3b). In agreement with previous late Quaternary

578   sedimentological and geochemical studies from the western Arctic (Darby et al., 2009), we

579   hypothesize that end-member EM3 recorded in the Holocene sediments from the Chukchi-

580   Alaskan margin may reflect suspended load and winnowed silts deposited by downwelling of

581   brine-enriched shelf waters. Moreover, the SedUnMixMC modelling reveals that sediment

582   provenance in core 05JPC was mainly derived from the Bering Strait, Mackenzie River and

583   Eurasian margin (Figures 7g-h). The proportion of sediment derived from the Mackenzie River

584   gradually decreases up-core (60 to 30%), whereas the Bering Strait and Eurasian margin sources

585   show a long-term increase (10 to 60% and 0 to 30%; Figures 7i-j). Indeed, decreases of quartz,

586   kaolinite, illite, aluminum and potassium contents most likely reflect a decline in sediment inputs

587   from the Mackenzie River (Figure 7), while an increase of total feldspars, chlorite, muscovite,

588   and vermiculite, as well as magnesium and iron contents in the clay fraction reflect higher Bering

589   Strait sediment inputs (Figures 7d-e, S5). Thus, the Holocene variations observed in the detrital

590   proxies from core 05JPC are likely related to a long-term decline in both the Mackenzie River

591   discharge (Wagner et al., 2011) and anchor ice transported by weaker BG (Yamamoto et al.,

26

592   2017). In addition, the increased proportion of sediment coming from the Kara Sea observed in

593   core 05JPC between 4 and 2 ka cal BP (15-30%; Figure 7g) suggests that a strong positive mode

594   of the AO was predominant at this time (Darby et al., 2012). In fact, based on iron oxide grain

595   provenance on the Chukchi shelf and slope sediments, Darby & Bischof (2004) and Darby et al.

596   (2012) suggested a weaker BG during the late Holocene, which also occurs today during the

597   positive phase of the AO in agreement with our interpretations (Figure 10).

598

599   As shown in Figures 7a-b-g and Figures 9c-d, the proportion of chlorite, vermiculite, total

600   feldspars, amorphous silica and sediments derived from the Bering Strait showed a gradual

601   increase between 10 and 2 ka cal BP, with maximum values recorded between 7.5 and 2 ka cal

602   BP, suggesting an enhanced increase in the Bearing Strait inflow into the Chukchi Sea. This

603   increased Bearing Strait inflow trend shows a parallel temporal evolution with regional sea level

604   variations and increasing bottom current redistribution (Figures 3-9). In agreement with Keigwin

605   et al. (2006), we hypothesize that the progressive and rapid relative sea-level rise observed during

606   10 and 7.5 ka cal BP in the western Arctic Ocean not only promoted the widening and deepening

607   of the Bering Strait, but also the subsequent remobilization of sediments stored on the Chukchi

608   Shelf and the enhanced sediment transport from the Pacific towards the western Arctic Ocean

609   (Figure 10). Our findings are consistent with palynological (dinocyt, pollen and spores) and

610   organic matter geochemistry data from the same sediment core (Faux et al., 2011; Khim, 2003;

611   McKay et al., 2008; Polyak et al., 2016), indicating that full marine continental shelf setting was

612   established in the Chukchi-Alaskan margin between 7 and 8 ka cal BP. Overall, these

613   observations suggest that regional sea level variations have exerted a significant control on

614   sedimentation in the western Arctic Ocean during the early- to mid-Holocene.

615

27

616 As a whole, although the variations in the previously published mineralogical proxy records of

617 the Bearing Strait inflow are not identical among the different sediment cores from the Chukchi

618 Sea (Figures 9e-i; Ortiz et al., 2009; Stein et al., 2017; Yamamoto et al., 2017), there is a

619 common enhancement in the Bering Strait inflow between 7.5 and 2 ka cal BP, followed by a

620 decrease during the last 2 ka cal BP (Ortiz et al., 2009; Stein et al., 2017; Yamamoto et al., 2017).

621 Holocene changes in the Bering Strait inflow have been attributed to changes in the Aleutian Low

622 pressure system, which is located in the North Pacific (Yamamoto et al., 2017). This Aleutian

623 Low is sensitive to tropical Pacific sea surface temperature (SST) anomalies (Anderson et al.,

624 2016; Osterberg et al., 2014; Trenberth & Hurrell, 1994). In general, warm eastern Pacific SST

625 conditions are characterized by a stronger and southeastward-shifted Aleutian Low, while cool

626 eastern Pacific SSTs conditions are associated with a weaker and northwestward-shifted Aleutian

627 Low. In this context, the Holocene paleoenvironmental records across eastern Beringia (Alaska,

628 westernmost Canada and adjacent seas) suggest that the Aleutian Low was weaker during the

629 middle Holocene than during the late Holocene (Barron & Anderson, 2011). This configuration is

630 thought to promote a major Bering Strait inflow into the Chukchi Sea during the middle

631 Holocene and a weak inflow during the late Holocene. Finally, as discussed in Darby & Bischof

632 (2004) and Yamamoto et al. (2017), sediments transported by the inflowing Pacific waters into

633 the Bering Strait might be diverted west towards Herald Canyon by the western Bering Sea

634 branches, and thus missing the Chukchi-Alaskan margin (Yamamoto et al., 2017). This

635 redistribution of the Bering Strait inflow between the different current branches may be a

636 plausible explanation for the spatial and temporal differences observed between the Pacific

637 inflow proxies from the Chukchi Sea cores (Figure 9).

28

6 Summary and conclusions

Geochemical and mineralogical compositions of two sediment cores recovered on the Canadian Beaufort (core 02PC) and Chukchi-Alaskan (core 05JPC) margins highlight the evolution of the origin, transport, and dynamics of the detrital sediments in the western Arctic Ocean since deglaciation. Overall, the results of this research yield the following generalizations and conclusions:

1. The end-member modelling analysis of grain-size data indicate that sea ice and nepheloid current are factors controlling sediment redistribution in the Chukchi-Alaskan margin, whereas sea ice and the Mackenzie River sediment plume influenced sedimentation in the Canadian Beaufort margin.

2. The mineralogical and geochemical data from the bulk and clay fractions corroborate that Log(I+K/C+V), Log(Qz/Fsp), dolomite, Log(Ca/Al), Log(Mg/Al), and Log(Fe/Al), together with a discriminant diagram based on Al–Si–Ca and I+K–total feldspars–dolomite, can be successfully used to track changes in detrital sediment provenance on the Chukchi and Beaufort continental margins.

3. The sediment unmixing model, together with specific mineralogical and geochemical signatures, indicates that the North American margin (including the Mackenzie River, Northern Alaska and Canadian Arctic Archipelago) is the major source of sediment during the deglaciation at the coring sites of cores 05JPC and 02PC.

4. The dolomite-rich IRD layers dated to 12.8 ka cal BP and 11 ka cal BP in core 02PC and 9.5 ka cal BP in core 05JPC are related to the debacle of the M'Clure and Amundsen Ice Streams. The quartz and feldspar-rich IRD intervals dated to 13 ka cal BP in core 02PC and 10.7 ka cal BP

29

660   in core 05JPC are likely related to meltwater events, and are derived from the Mackenzie River

661   and the Brooks Range glaciers in the northwestern Alaska, respectively.

662   5. Mineralogical and geochemical signatures of deglacial sediments from core 02PC support the

663   hypothesis that large meltwater and iceberg discharges from the Lake Agassiz outburst through

664   the Mackenzie Valley may have triggered the Younger Dryas cooling.

665   6. During the Holocene, the detrital sediment supply in the Canadian Beaufort margin remains

666   controlled mainly by the Mackenzie River. In the Chukchi margin, the proportion of sediment

667   derived from the Mackenzie River gradually decreased during the early to late Holocene.

668   7. The opening of the Bering Strait at 11 ka cal BP is typified in core 05JPC by a sharp increase

669   in vermiculite, mixed-layer chlorite/smectite and amorphous silica. In addition, bulk

670   mineralogical data, together with high Log(Mg/Al) and Log(Fe/Al) ratios from the clay fraction,

671   supports the notion that an enhanced Bearing Strait inflow into the Chukchi Sea occurred

672   between 7.5 to 2 ka cal BP.

673   8. The similar trends observed between the regional sea-level curves and our mineralogical and

674   geochemical data suggest that the relative sea-level changes in the western Arctic Ocean have an

675   important influence on the western Arctic sedimentary dynamics during the early to mid-

676   Holocene.

677

678   **Acknowledgments**

30

7   References

691

692 Aitchison, J. (1990). Relative variation diagrams for describing patterns of compositional
693   variability. *Mathematical Geology, 22*, 487-511. doi: 10.1007/BF00890330

694 Anderson, L., Berkelhammer, M., Barron, J. A., Steinman, B. A., Finney, B. P. & Abbott, M. B.
695   (2016). Lake oxygen isotopes as recorders of North American Rocky Mountain
696   hydroclimate: Holocene patterns and variability at multi-decadal to millennial time scales.
697   *Global and Planetary Change, 137*, 131-148. doi: 10.1016/j.gloplacha.2015.12.021

698 Andrews, J. T. (2000). Icebergs and iceberg rafted detritus (IRD) in the North Atlantic: facts and
699   assumptions. *Oceanography, 13*, 100-108.

700 Andrews, J. T., Bjork, A. A., Eberl, D. D., Jennings, A. E. & Verplanck, E. P. (2015). Significant
701   differences in late Quaternary bedrock erosion and transport: East versus West Greenland
702   ~70°N - evidence from the mineralogy of offshore glacial marine sediments. *Journal of*
703   *Quaternary Science, 30*, 452-463. doi: 10.1002/jqs.2787

704 Andrews, J. T. & Eberl, D. D. (2012). Determination of sediment provenance by unmixing the
705   mineralogy of source-area sediments: The "SedUnMix" program. *Marine Geology, 291-*
706   *294*, 24-33. doi: 10.1016/j.margeo.2011.10.007

707 Andrews, J. T., Stein, R., Moros, M. & Perner, K. (2016). Late Quaternary changes in sediment
708   composition on the NE Greenland margin (~73° N) with a focus on the fjords and shelf.
709   *Boreas, 45*, 381-397. doi: 10.1111/bor.12169

710 Andrews, J. T. & Vogt, C. (2014). Source to sink: Statistical identification of regional variations
711   in the mineralogy of surface sediments in the western Nordic Seas (58°N–75°N; 10°W–
712   40°W). *Marine Geology, 357*, 151-162. doi: 10.1016/j.margeo.2014.08.005

713 Asahara, Y., Takeuchi, F., Nagashima, K., Harada, N., Yamamoto, K., Oguri, K. & Tadai, O.
714   (2012). Provenance of terrigenous detritus of the surface sediments in the Bering and
715   Chukchi Seas as derived from Sr and Nd isotopes: Implications for recent climate change
716   in the Arctic regions. *Deep-Sea Research Part II: Topical Studies in Oceanography, 61-*
717   *64*, 155-171. doi: 10.1016/j.dsr2.2011.12.004

Barletta, F., St-Onge, G., Channell, J. E. T., Rochon, A., Polyak, L. & Darby, D. (2008). High-resolution paleomagnetic secular variation and relative paleointensity records from the western Canadian Arctic: implication for Holocene stratigraphy and geomagnetic field behaviour. *Canadian Journal of Earth Sciences, 45*, 1265-1281. doi: 10.1139/E08-039

Barron, J. A. & Anderson, L. (2011). Enhanced Late Holocene ENSO/PDO expression along the margins of the eastern North Pacific. *Quaternary International, 235*, 3-12. doi: 10.1016/j.quaint.2010.02.026

Belt, S. T., Vare, L. L., Massé, G., Manners, H. R., Price, J. C., MacLachlan, S. E., Andrews, J. T. & Schmidt, S. (2010). Striking similarities in temporal changes to spring sea ice occurrence across the central Canadian Arctic Archipelago over the last 7000 years. *Quaternary Science Reviews, 29*, 3489-3504. doi: 10.1016/j.quascirev.2010.06.041

Biscaye, P. E. (1965). Mineralogy and Sedimentation of Recent Deep-Sea Clay in the Atlantic Ocean and Adjacent Seas and Oceans. *Geological Society of America Bulletin, 76*, 803-832. doi: 10.1130/0016-7606(1965)76

Bischof, J. F. & Darby, D. A. (1999). Quaternary ice transport in the Canadian Arctic and extent of Late Wisconsinan Glaciation in the Queen Elizabeth Islands. *Canadian Journal of Earth Sciences, 36*, 2007-2020. doi: 10.1139/e99-096

Blott, S. J. & Pye, K. (2001). GRADISTAT: A Grain Size Distribution and Statistic Package For the Analysis of Unconsolidated Sediments. *Earth Surface Processes and Landforms, 26*, 1237-1248.

Bout-Roumazeilles, V., Cortijo, E., Labeyrie, L. & Debrabant, P. (1999). Clay mineral evidence of nepheloid layer contributions to the Heinrich layers in the northwest Atlantic. *Palaeogeography, Palaeoclimatology, Palaeoecology, 146*, 211-228. doi: 10.1016/S0031-0182(98)00137-0

Condron, A. & Winsor, P. (2012). Meltwater routing and the Younger Dryas. *Proceedings of the National Academy of Sciences, 109*, 19928-19933. doi: 10.1073/pnas.1207381109

Coulthard, R. D., Furze, M. F. A., Pieńkowski, A. J., Chantel Nixon, F. & England, J. H. (2010). New marine ΔR values for Arctic Canada. *Quaternary Geochronology, 5*, 419-434. doi: 10.1016/j.quageo.2010.03.002

Danielson, S. L., Weingartner, T. J., Hedstrom, K. S., Aagaard, K., Woodgate, R., Curchitser, E. & Stabeno, P. J. (2014). Coupled wind-forced controls of the Bering–Chukchi shelf circulation and the Bering Strait throughflow: Ekman transport, continental shelf waves, and variations of the Pacific–Arctic sea surface height gradient. *Progress in Oceanography, 125*, 40-61. doi: 10.1016/j.pocean.2014.04.006

Darby & Bischof (2004). A Holocene record of changing Arctic Ocean ice drift analogous to the effects of the Arctic Oscillation. *Paleoceanography, 19*, 1-9. doi: 10.1029/2003PA000961

Darby, D. A., Jakobsson, M. & Polyak, L. (2005). Icebreaker expedition collects key Arctic seafloor and ice data. *Eos, Transactions American Geophysical Union, 86*, 549-549. doi: 10.1029/2005EO520001

Darby, D. A., Myers, W. B., Jakobsson, M. & Rigor, I. (2011). Modern dirty sea ice characteristics and sources: The role of anchor ice. *Journal of Geophysical Research: Oceans, 116*, 1-18. doi: 10.1029/2010JC006675

Darby, D. A., Ortiz, J., Polyak, L., Lund, S., Jakobsson, M. & Woodgate, R. A. (2009). The role of currents and sea ice in both slowly deposited central Arctic and rapidly deposited Chukchi-Alaskan margin sediments. *Global and Planetary Change, 68*, 58-72. doi: 10.1016/j.gloplacha.2009.02.007

764   Darby, D. A., Ortiz, J. D., Grosch, C. E. & Lund, S. P. (2012). 1,500-year cycle in the Arctic
765   Oscillation identified in Holocene Arctic sea-ice drift. *Nature Geoscience, 5*, 897-900.
766   doi: 10.1038/ngeo1629

767   Darby, D. A. & Zimmerman, P. (2008). Ice-rafted detritus events in the Arctic during the last
768   glacial interval, and the timing of the Innuitian and Laurentide ice sheet calving events.
769   *Polar Research, 27*, 114-127. doi: 10.1111/j.1751-8369.2008.00057.x

770   Dellinger, M., Bouchez, J., Gaillardet, J., Faure, L. & Moureau, J. (2017). Tracing weathering
771   regimes using the lithium isotope composition of detrital sediments. *Geology, 45*, 411-
772   414. doi: 10.1130/G38671.1

773   Deschamps, C.-E., St-Onge, G., Montero-Serrano, J.-C. & Polyak, L. (2017). Chronostratigraphy
774   and spatial distribution of the Chukchi and Beaufort Sea's magnetic sediments since the
775   last deglaciation. *Boreas*. doi:10.1111/bor.12296

776   Dietze, E., Hartmann, K., Diekmann, B., Ijmker, J., Lehmkuhl, F., Opitz, S., Stauch, G.,
777   Wünnemann, B. & Borchers, A. (2012). An end-member algorithm for deciphering
778   modern detrital processes from lake sediments of Lake Donggi Cona, NE Tibetan Plateau,
779   China. *Sedimentary Geology, 243-244*, 169-180. doi: 10.1016/j.sedgeo.2011.09.014

780   Dyke, A. S. & Savelle, J. M. (2000). Major end moraines of Younger Dryas age on Wollaston
781   Peninsula, Victoria Island, Canadian Arctic: implications for paleoclimate and for
782   formation of hummocky moraine. *Canadian Journal of Earth Sciences, 38*, 601-619. doi:
783   10.1139/cjes-38-6-1003

784   Eberl, D. D. (2003). User guide to RockJock—A program for determining quantitative
785   mineralogy from X-ray diffraction data. *USGS Open File Report, OF 03-78*, 40.

786   El Ouahabi, M., Hubert-Ferrari, A. & Fagel, N. (2017). Lacustrine clay mineral assemblages as a
787   proxy for land-use and climate changes over the last 4 kyr: The Amik Lake case study,
788   Southern Turkey. *Quaternary International, 438*, 15-29. doi:
789   10.1016/j.quaint.2016.11.032

790   Elias, S. A., Short, S. K. & Phillips, R. L. (1992). Paleoecology of Late-Glacial Peats from the
791   Bering Land Bridge, Chukchi Sea Shelf Region, Northwestern Alaska. *Quaternary*
792   *Research, 38*, 371-378. doi: 10.1016/0033-5894(92)90045-K

793   England, J. H. & Furze, M. F. A. (2008). New evidence from the western Canadian Arctic
794   Archipelago for the resubmergence of Bering Strait. *Quaternary Research, 70*, 60-67. doi:
795   10.1016/j.yqres.2008.03.001

796   Fagel, N., Not, C., Gueibe, J., Mattielli, N. & Bazhenova, E. (2014). Late Quaternary evolution of
797   sediment provenances in the Central Arctic Ocean: Mineral assemblage, trace element
798   composition and Nd and Pb isotope fingerprints of detrital fraction from the Northern
799   Mendeleev Ridge. *Quaternary Science Reviews, 92*, 140-154. doi:
800   10.1016/j.quascirev.2013.12.011

801   Faux, J. F., Belicka, L. L. & Rodger Harvey, H. (2011). Organic sources and carbon sequestration
802   in Holocene shelf sediments from the western Arctic Ocean. *Continental Shelf Research,*
803   *31*, 1169-1179. doi: 10.1016/j.csr.2011.04.001

804   Forest, A., Tremblay, J. é., Gratton, Y., Martin, J., Gagnon, J., Darnis, G., Sampei, M., Fortier,
805   L., Ardyna, M., Gosselin, M., Hattori, H., Nguyen, D., Maranger, R., Vaqué, D., Marrasé,
806   C., Pedrós-Alió, C., Sallon, A., Michel, C., Kellogg, C., Deming, J., Shadwick, E.,
807   Thomas, H., Link, H., Archambault, P. & Piepenburg, D. (2011). Biogenic carbon flows
808   through the planktonic food web of the Amundsen Gulf (Arctic Ocean): A synthesis of
809   field measurements and inverse modeling analyses. *Progress in Oceanography, 91*, 410-
810   436. doi: 10.1016/j.pocean.2011.05.002

33

811   Gajewski, K. (2015). Quantitative reconstruction of Holocene temperatures across the Canadian
812   Arctic and Greenland. *Global and Planetary Change, 128*, 14-23. doi:
813   10.1016/j.gloplacha.2015.02.003
814   Gamboa, A. 2017: Evaluación de la dinámica sedimentaria del margen continental del mar de
815   Beaufort y golfo de Amundsen (Océano Ártico): implicaciones paleoceanográficas y
816   paleoclimáticas durante el Holoceno. Universidad de Oriente. 240 pp.
817   Gamboa, A., Montero-Serrano, J.-C., St-Onge, G., Rochon, A. & Desiage, P.-A. (2017).
818   Mineralogical, geochemical and magnetic signatures of surface sediments from the
819   Canadian Beaufort Shelf and Amundsen Gulf (Canadian Arctic). *Geochemistry,
820   Geophysics, Geosystems, 18*, 488-512. doi: 10.1002/2016GC006477
821   Hamilton, T. D. 1986: Late Cenozoic glaciation of the central Brooks Range. *Glaciation in
822   Alaska; the geologic record* (ed. by T.D. Hamilton, K.M. Reed and R.M. Thorson).
823   Alaska Geological Society. Anchorage. 9-49.
824   Hanslik, D., Jakobsson, M., Backman, J., Björck, S., Sellén, E., O'Regan, M., Fornaciari, E. &
825   Skog, G. (2010). Quaternary Arctic Ocean sea ice variations and radiocarbon reservoir
826   age corrections. *Quaternary Science Reviews, 29*, 3430-3441. doi:
827   10.1016/j.quascirev.2010.06.011
828   Harrison, J. C., St-Onge, M. R., Petrov, O. V., Strelnikov, S. I., Lopatin, B. G., Wilson, F. H.,
829   Tella, S., Paul, D., Lynds, T., Shokalsky, S. P., Hults, C. K., Bergman, S., Jepsen, H. F. &
830   Solli, A. (2011). Geological map of the Arctic. *Geological Survey of Canada Open File,
831   5816*.
832   Héquette, A., Marie-Hélène, R. & Hill, P. R. (1995). The effects of the Holocene Sea Level Rise
833   on the Evolution of the Southeastern Coast of the Canadian Beaufort Sea. *Journal of
834   Coastal Research, 11*, 494-507.
835   Hill, J. C. & Driscoll, N. W. (2008). Paleodrainage on the Chukchi shelf reveals sea level history
836   and meltwater discharge. *Marine Geology, 254*, 129-151. doi:
837   10.1016/j.margeo.2008.05.018
838   Hill, J. C. & Driscoll, N. W. (2010). Iceberg discharge to the Chukchi shelf during the Younger
839   Dryas. *Quaternary Research, 74*, 57-62. doi: 10.1016/j.yqres.2010.03.008
840   Hillaire-Marcel, C., Maccali, J., Not, C. & Poirier, A. (2013). Geochemical and isotopic tracers of
841   Arctic sea ice sources and export with special attention to the Younger Dryas interval.
842   *Quaternary Science Reviews, 79*, 184-190. doi: 10.1016/j.quascirev.2013.05.001
843   Jakobsson, M., Pearce, C., Cronin, T. M., Backman, J., Anderson, L. G., Barrientos, N., Björk,
844   G., Coxall, H., de Boer, A., Mayer, L. A., Mörth, C.-M., Nilsson, J., Rattray, J. E.,
845   Stranne, C., Semilietov, I., amp, apos & Regan, M. (2017). Post-glacial flooding of the
846   Beringia Land Bridge dated to 11,000 cal yrs BP based on new
847   geophysical and sediment records. *Climate of the Past Discussions, 13*, 991-1005. doi:
848   10.5194/cp-13-991-2017
849   Jombart, T. (2008). Adegenet: A R package for the multivariate analysis of genetic markers.
850   *Bioinformatics, 24*, 1403-1405. doi: 10.1093/bioinformatics/btn129
851   Kalinenko, V. V. (2001). Clay Minerals in Sediments of the Arctic Seas. *Lithology and Mineral
852   Resources, 36*, 362-372. doi: 10.1023/A:1010414305264
853   Keigwin, L. D., Donnelly, J. P., Cook, M. S., Driscoll, N. W. & Brigham-Grette, J. (2006). Rapid
854   sea-level rise and Holocene climate in the Chukchi Sea. *Geology, 34*, 861-864. doi:
855   10.1130/G22712.1

34

856 Khim, B. K. (2003). Two modes of clay-mineral dispersal pathways on the continental shelves of
857   the East Siberian Sea and western Chukchi Sea. *Geosciences Journal, 7*, 253-262. doi:
858   10.1007/BF02910292
859 Kobayashi, D., Yamamoto, M., Irino, T., Nam, S.-I., Park, Y.-H., Harada, N., Nagashima, K.,
860   Chikita, K. & Saitoh, S.-I. (2016). Distribution of detrital minerals and sediment color in
861   western Arctic Ocean and northern Bering Sea sediments: Changes in the provenance of
862   western Arctic Ocean sediments since the last glacial period. *Polar Science, 10*, 519-531.
863   doi: 10.1016/j.polar.2016.07.005
864 Krumm, S. (2006). SediCalc (Free Geological Software).
865 Krylov, A. A., Stein, R. & Ermakova, L. A. (2014). Clay minerals as indicators of late quaternary
866   sedimentation constraints in the Mendeleev Rise, Amerasian Basin, Arctic Ocean.
867   *Lithology and Mineral Resources, 49*, 103-116. doi: 10.1134/S0024490213060059
868 Lakeman, T. R., Pie, A. J., Nixon, F. C., Furze, M. F. A., Blasco, S., Andrews, J. T. & King, E.
869   L. (2018). Collapse of a marine-based ice stream during the early Younger Dryas
870   chronozone , western Canadian Arctic. *46*, 1-4. doi: 10.1130/G39665.1
871 Lambeck, K., Rouby, H., Purcell, A., Sun, Y. & Sambridge, M. (2014). Sea level and global ice
872   volumes from the Last Glacial Maximum to the Holocene. *Proceedings of the National
873   Academy of Sciences, 111*, 15296-15303. doi: 10.1073/pnas.1411762111
874 Lisé-Pronovost, A., St-Onge, G., Brachfeld, S., Barletta, F. & Darby, D. (2009). Paleomagnetic
875   constraints on the Holocene stratigraphy of the Arctic Alaskan margin. *Global and
876   Planetary Change, 68*, 85-99. doi: 10.1016/j.gloplacha.2009.03.015
877 Maccali, J., Hillaire-Marcel, C., Carignan, J. & Reisberg, L. C. (2013). Geochemical signatures
878   of sediments documenting Arctic sea-ice and water mass export through Fram Strait since
879   the Last Glacial Maximum. *Quaternary Science Reviews, 64*, 136-151. doi:
880   10.1016/j.quascirev.2012.10.029
881 McKay, J. L., de Vernal, A., Hillaire-Marcel, C., Not, C., Polyak, L. & Darby, D. (2008).
882   Holocene fluctuations in Arctic sea-ice cover: dinocyst-based reconstructions for the
883   eastern Chukchi Sea. *Canadian Journal of Earth Sciences, 45*, 1377-1397. doi:
884   10.1139/E08-046
885 Millot, R., Gaillardet, J., Dupré, B. & Allégre, C. J. (2003). Northern latitude chemical
886   weathering rates: Clues from the Mackenzie River Basin, Canada. *Geochimica et
887   Cosmochimica Acta, 67*, 1305-1329. doi: 10.1016/S0016-7037(02)01207-3
888 Montero-Serrano, J. C., Deschamps, C.-E. & Jaegle, M. 2014: Amundsen Expedition Report:
889   Geology and paleoceanography leg 2a. ArctiNet, Université Laval.
890 Naidu, A. S., Burrell, D. C. & Hood, D. W. (1971). Clay mineral composition and geological
891   significance of some Beaufort Sea sediments. *Journal of Sedimentary Petrology, 41*, 691-
892   694. doi: 10.1306/74D72329-2B21-11D7-8648000102C1865D
893 Naidu, A. S., Creager, J. S. & Mowatt, T. C. (1982). Clay mineral dispersal patterns in the north
894   Bering and Chukchi Seas. *Marine Geology, 47*, 1-15. doi: 10.1016/0025-3227(82)90016-
895   0
896 Naidu, A. S. & Mowatt, T. C. (1983). Sources and dispersal patterns of clay minerals in surface
897   sediments from the continental-shelf areas off Alaska. *Geological Society of America
898   Bulletin, 94*, 841-854. doi: 10.1130/0016-7606(1983)94
899 Not, C. & Hillaire-Marcel, C. (2012). Enhanced sea-ice export from the Arctic during the
900   Younger Dryas. *Nature Communications, 3*, 647-647. doi:
901   10.1016/j.marchem.2011.12.005

902 Ortiz, J. D., Polyak, L., Grebmeier, J. M., Darby, D., Eberl, D. D., Naidu, S. & Nof, D. (2009).
903   Provenance of Holocene sediment on the Chukchi-Alaskan margin based on combined
904   diffuse spectral reflectance and quantitative X-Ray Diffraction analysis. *Global and*
905   *Planetary Change, 68*, 73-84. doi: 10.1016/j.gloplacha.2009.03.020
906 Osterberg, E. C., Mayewski, P. A., Fisher, D. A., Kreutz, K. J., Maasch, K. A., Sneed, S. B. &
907   Kelsey, E. (2014). Mount Logan ice core record of tropical and solar influences on
908   Aleutian Low variability: 500–1998 A.D. *Journal of Geophysical Research: Atmospheres*
909   *Research, 119*, 11,189-111,204. doi: 10.1002/2014JD021847
910 Overland, J. E., Adams, J. M., Bond, N. A., Climate, J. O. F., Marine, P., Overland, J. E., Adams,
911   J. M., Bond, N. A., Climate, J. O. F. & Marine, P. (1999). Decadal Variability of the
912   Aleutian Low and Its Relation to High-Latitude Circulation. *Journal of Climate, 12*, 1542-
913   1548. doi: 10.1175/1520-0442(1999)012
914 Padgham, W. A. & Fyson, W. K. (1992). The Slave Province: a distinct Archean craton.
915   *Canadian Journal of Earth Sciences, 29*, 2072-2086. doi: 10.1139/e92-165
916 Petschick, R. (2000). MacDiff 4.2. 5 Manual. *Institut für Geologie, Universität Erlangen:*
917   *Germany*.
918 Pickart, R. S. (2004). Shelfbreak circulation in the Alaskan Beaufort Sea: Mean structure and
919   variability. *Journal of Geophysical Research C: Oceans, 109*, 1-14. doi:
920   10.1029/2003JC001912
921 Polyak, L., Belt, S. T., Cabedo-Sanz, P., Yamamoto, M. & Park, Y. H. (2016). Holocene sea-ice
922   conditions and circulation at the Chukchi-Alaskan margin, Arctic Ocean, inferred from
923   biomarker proxies. *The Holocene, 26*, 1-12. doi: 10.1177/0959683616645939
924 Polyak, L., Darby, D. A., Bischof, J. F. & Jakobsson, M. (2007). Stratigraphic constraints on late
925   Pleistocene glacial erosion and deglaciation of the Chukchi margin, Arctic Ocean.
926   *Quaternary Research, 67*, 234-245. doi: 10.1016/j.yqres.2006.08.001
927 Pourmand, A., Dauphas, N. & Ireland, T. J. (2012). A novel extraction chromatography and MC-
928   ICP-MS technique for rapid analysis of REE, Sc and Y: Revising CI-chondrite and Post-
929   Archean Australian Shale (PAAS) abundances. *Chemical Geology, 291*, 38-54. doi:
930   10.1016/j.chemgeo.2011.08.011
931 Reimer, P. J., Bard, E., Bayliss, A., Beck, J. W., Blackwell, P. G., Ramsey, C. B., Buck, C. E.,
932   Cheng, H., Edwards, R. L., Friedrich, M., Grootes, P. M., Guilderson, T. P., Haflidison,
933   H., Hajdas, I., Hatté, C., Heaton, T., Hoffmann, D. L., Hogg, A., Hughen, K. A., Kaiser,
934   K., Kromer, B., Manning, S. W., Niu, M., Reimer, R., Richards, D. A., Scott, E. M.,
935   Southon, J. R., Staff, R. A., Turney, C. & Plicht, J. (2013). IntCal13 and Marine13
936   radiocarbon age calibration curves 0-50,000 years cal BP. *Radiocarbon, 55*, 1869-1887.
937   doi: 10.2458/azu_js_rc.55.16947
938 Schoster, F., Behrends, M., Muller, R., Stein, R. & Washner, M. (2000). Modern river discharge
939   and pathways of supplied material in the Eurasian Arctic Ocean: Evidence from mineral
940   assemblagesand major and minor element distribution. *International Journal of Earth*
941   *Sciences, 89*, 486-495. doi: 10.1007/s005310000120
942 Scott, D. B., Schell, T., St-Onge, G., Rochon, A. & Blasco, S. (2009). Foraminiferal assemblage
943   changes over the last 15,000 years on the Mackenzie-Beaufort Sea Slope and Amundsen
944   Gulf, Canada: Implications for past sea ice conditions. *Paleoceanography, 24*, 1-20. doi:
945   10.1029/2007PA001575
946 Stein, R., Fahl, K., Schade, I., Manerung, A., Wassmuth, S., Niessen, F. & Nam, S.-I. (2017).
947   Holocene variability in sea ice cover, primary production, and Pacific-Water inflow and

climate change in the Chukchi and East Siberian Seas (Arctic Ocean). *Journal of Quaternary Science, 32*, 362-379. doi: 10.1002/jqs.2929

Stokes, C. R., Clark, C. D., Darby, D. A. & Hodgson, D. A. (2005). Late Pleistocene ice export events into the Arctic Ocean from the M'Clure Strait Ice Stream, Canadian Arctic Archipelago. *Global and Planetary Change, 49*, 139-162. doi: 10.1016/j.gloplacha.2005.06.001

Stokes, C. R., Clark, C. D. & Storrar, R. (2009). Major changes in ice stream dynamics during deglaciation of the north-western margin of the Laurentide Ice Sheet. *Quaternary Science Reviews, 28*, 721-738. doi: 10.1016/j.quascirev.2008.07.019

Stokes, C. R., Clark, C. D. & Winsborrow, C. M. (2006). Subglacial bedform evidence for a major palaeo-ice stream and its retreat phases in Amundsen Gulf, Canadian Arctic Archipelago. *Journal of Quaternary Science, 21*, 399-412. doi: 10.1002/jqs.991

Tarasov, L. & Peltier, W. R. (2005). Arctic freshwater forcing of the Younger Dryas cold reversal. *Nature, 435*, 662-665. doi: 10.1038/nature03617

Tremblay, L. B., Mysak, L. A. & Dyke, A. S. (1997). Evidence from driftwood records for century-to-millennial scale variations of the high latitude atmospheric circulation during the Holocene. *Geophysical Research Letters, 24*, 2027-2030. doi: 10.1029/97GL02028

Trenberth, K. E. & Hurrell, J. W. (1994). Decadal atmospheric-ocean variations in the Pacific. *Climate Dynamics, 9*, 303-319. doi: 10.1007/BF00204745

van Den Boogaart, K. G. & Tolosana-Delgado, R. (2008). "compositions": A unified R package to analyze compositional data. *Computers and Geosciences, 34*, 320-338. doi: 10.1016/j.cageo.2006.11.017

van Den Boogaart, K. G. & Tolosana-Delgado, R. 2013: *Analyzing Compositional Data with R.* 273 pp. Springer, Heidelberg-New York-Dodrecht-London. doi: 10.1007/978-3-642-36809-7

Viscosi-Shirley, C., Pisias, N. & Mammone, K. (2003). Sediment source strength, transport pathways and accumulation patterns on the Siberian-Arctic's Chukchi and Laptev shelves. *Continental Shelf Research, 23*, 1201-1225. doi: 10.1016/S0278-4343(03)00090-6

Vogt, C. 1997: Regional and temporal variations of mineral assemblages in Arctic Ocean sediments as climatic indicator during glacial/ interglacial changes.

von Eynatten, H., Tolosana-Delgado, R. & Karius, V. (2012). Sediment generation in modern glacial settings: Grain-size and source-rock control on sediment composition. *Sedimentary Geology, 280*, 80-92. doi: 10.1016/j.sedgeo.2012.03.008

Wagner, A., Lohmann, G. & Prange, M. (2011). Arctic river discharge trends since 7ka BP. *Global and Planetary Change, 79*, 48-60. doi: 10.1016/j.gloplacha.2011.07.006

Wahsner, M., Müller, C., Stein, R., Ivanov, G., Levitan, M., Shelekhova, E. & Tarasov, G. (1999). Clay-mineral distribution in surface sediments of the Eurasian Arctic Ocean and continental margin as indicator for source areas and transport pathways - a synthesis. *Boreas, 28*, 215-233. doi: 10.1111/j.1502-3885.1999.tb00216.x

Weingartner, T., Aagaard, K., Woodgate, R., Danielson, S., Sasaki, Y. & Cavalieri, D. (2005). Circulation on the north central Chukchi Sea shelf. *Deep Sea Research Part II: Topical Studies in Oceanography, 52*, 3150-3174. doi: 10.1016/j.dsr2.2005.10.009

Weltje, G. J. (1997). End-member modeling of compositional data: Numerical-statistical algorithms for solving the explicit mixing problem. *Mathematical Geology, 29*, 503-549. doi: 10.1007/BF02775085

993 Wickert, A. D. (2016). Reconstruction of North American drainage basins and river discharge
994 since the Last Glacial Maximum. *Earth Surface Dynamics, 4*, 831-869. doi:
995 10.5194/esurf-4-831-2016
996 Yamamoto, M., Nam, S.-I., Polyak, L., Kobayashi, D., Suzuki, K., Irino, T. & Shimada, K.
997 (2017). Holocene dynamics in the Bering Strait inflow to the Arctic and the Beaufort
998 Gyre circulation based on sedimentary records from the Chukchi Sea. *Climate of the Past,*
999 *13*, 1111-1127. doi: 10.5194/cp-13-1111-2017

8 Figure captions

Figure 1. (a) Schematic map of Arctic oceanic circulation and localization of the mineralogical (red circle) and geochemical (white circle). (b) Localization of cores 05JPC and 02PC (this study) as well as cores 56PC (Lakeman et al., 2018), 750PC (Scott et al., 2009), ARA2B-A1 (Yamamoto et al., 2017), ARA2B-1B (Stein et al., 2017) and core 06JPC (Ortiz et al., 2009). References used for the geochemical and mineralogical database are listed in Table SM2.

Figure 2. (a) Discriminant function analyses (DFA) and (b) membership probability of the circum-Arctic sources based on log ratio mineral data. The membership probability diagram corroborates that potential sediment sources have different mineralogical characteristics that allow a reasonable degree of discrimination, as indicated by their relatively high membership value (up to 90%).

Figure 3. End-member modelling analyses (EMMA) performed on the grain-size distribution of the detrital fraction from cores 01JPC, 05JPC, 03PC and 02PC. (a) Three representative, unmixed grain-size distributions, as well as (b) end-member scores (%) derived from EMMA are shown.

Figure 4. (a) Al_2O_3-SiO_2-CaO ternary plot showing the overall composition (bulk and clay fractions) of the sediment from cores 05JPC and 02PC in comparison to the average shale and circum-Arctic source areas. (b) Kaolinite+Illite (K+I) – total feldspars (Fsp) – dolomite (Dol) ternary plot for cores 05JPC and 02PC based on bulk mineralogy. (c) Relationship between Log(Mg/K) and Log(Fe/Al) ratios derived from the clay fraction of sediment cores 05JPC (square) and 02PC (circle). The log ratio I+K/C is represented by a gradient color from high (red) to low (blue) values. (d) Log(Qz/Fsd) versus Log(I+K/Ch+Ms) diagram illustrating the bulk mineralogical difference between cores 02PC and 05JPC and some circum-Arctic regions. Geochemical and mineralogical data of the circum-Arctic regions are shown in Table SM2.

Figure 5. X-ray diffractograms of typical samples from cores 02PC and 05JPC showing interpretation of major clay mineral species from the three classical runs, i.e., in air-dried, glycolated, and heated conditions.

38

Figure 6. Downcore variations of core 02PC showing (a) log-ratio illite/kaolinite and dolomite content (red). (b) log-ratios quartz/feldspar (black) and phyllosilicates/feldspar (red). (c) log-ratio Zr/Al (black) and Ca/Al (red). (d) log-ratio Mg/Al for the bulk (black) and clay (red) fractions. (e) log-ratio Fe/Al for the bulk (black) and clay (red) fractions. (f) Magnetic susceptibility, k_{lf} (Deschamps et al., 2017). (g) Proportion of sediment from the Kara Sea (black). (h) Proportion of sediment from the Mackenzie River (black), Mackenzie River sand (blue) and CAA (red). IRD layers rich in dolomite and quartz are highlighted in gray and blue, respectively.

Figure 7. Downcore variations of core 05JPC showing (a) log-ratio illite+kaolinite/chlorite. (b) log-ratio quartz/feldspar (black) and proportion of dolomite (red). (c) log-ratio Zr/Al (black) and Ca/Al (red). (d) log-ratio Mg/Al for the bulk (black) and clay (red) fractions. (e) log-ratio Fe/Al for the bulk (black) and clay (red) fractions. (f) Magnetic susceptibility, k_{lf} (Barletta *et al*., 2008). (g) Proportion of sediment from the Eurasian margin (EM), which includes Kara Sea and Eastern Siberian Sea in green and proportion of sediment from the Bering Strait in black. (h) Proportion of sediment from the Mackenzie River (black), North Alaska (blue) and CAA (red). IRD layers rich in dolomite and quartz are highlighted in gray and blue, respectively.

Figure 8. (a) Phyllosilicates-plagioclase-K-feldspar ternary plot of sand samples from the main tributaries of the Mackenzie River (Gamboa, 2017). Note that the northern tributaries are enriched in phyllosilicates while the southern tributaries are enriched in total feldspars. (b) Comparison of Log(EM3/EM2), Log(EM1/EM2), Log(Qz/Fsd), dolomite content, Log(Phy/Fsd) and Log(I/K) from core 02PC with global eustatic sea level variations (Lambeck et al., 2014) and relative sea level from the Beaufort Sea (Héquette et al., 1995).

Figure 9. Comparison of (a) global eustatic sea level changes and relative sea level variation in the Beaufort Sea, (b) Log(EM1/EM2) for cores 05JPC, (c) log-ratio chlorite/illite based on bulk (black) and clay mineralogy (red) from core 05JPC, (d) Log-ratio chlorite+vermiculite/illite+kaolinite based on bulk (black) and clay mineralogy (red) from core 05JPC, (e) amorphous silica from core 05JPC (black) and biogenic opal for the core ARA2B-1A (blue), (f) Log-ratio chlorite/illite derived of the bulk mineralogy from core 05JPC, (g) Log-ratio chlorite/illite of the bulk mineralogy from core 06JPC, (h) Log-ratio chlorite/illite of the bulk mineralogy from core ARA2B-1A, (i) Chlorite+muscovite contents from core ARA2B-1B, and (j) Chlorite proxy obtained by diffusive spectral reflectance analysis from cores 06JPC/TC. Enhanced Bering Strait inflow is highlighted in gray and opening of the Bering Strait is highlighted in light green.

Figure 10. Evolution of sedimentary dynamics in the western Arctic Ocean during the last 13 ka cal BP.

Supplementary material

Figure S1. Downcore variations of the major-, minor-, and trace-elements measured on the bulk (square) and clay (diamond) fractions for cores (a) 02PC and (b) 05JPC. IRDs layers rich in dolomite and quartz are highlighted in gray and blue, respectively.

Figure S2. Downcore variations of the major mineralogical components determined for the cores (a) 02PC and (b) 05JPC. IRDs layers rich in dolomite and quartz are highlighted in light and dark gray, respectively.

Figure S3. Downcore variations of the clay minerals assemblages identified in the cores (a) 02PC and (b) 05JPC. IRDs layers rich in dolomite and quartz are highlighted in light and dark gray, respectively.

Figure S4. Relationship between (a) log-ratio chlorite+vermiculite/illite+kaolinite (black) and log-ratio Fe/Al (grey) and (b) log-ratio chlorite+vermiculite/illite+kaolinite (black) and Log(Mg/Al) derived from the clay fraction of the core 05JPC. The correlation was performed using the software Analyseries (Paillard *et al*., 1996). Red and blue lines are the mean values for the log-ratio Fe/Al and log-ratio Mg/Al for Unit I and II respectively. The increase of Fe and Mg in unit I are significant ($p < 0.05$) based on a Student's t-test.

Figure SM1. (a) Proposed correlations between cores 750PC (Scott et al., 2009), 56PC (Lakeman et al., 2018), 02PC (this study) from the Beaufort Sea as well as core 05JPC (this study) from the Chukchi Sea. (b) Age model and sedimentation rates of core 02PC based on the correlations in figure (a) and the paleomagnetic tie-points from Deschamps et al. (2017). Note that radiocarbon ages (blue circles) are shown in conventional ages.

Figure SM2. SedUnMixMC results of measured (known) and calculated (estimated) fractions of a series of mixed samples from 4 different sources bedrock and sediments. The samples used are granite from Canadian Shield, shale from the Appalachian Mountains, limestone from Quarry Island (Mingan Archipelago) and Fe-rich glacial till from SW Gulf of Saint Lawrence. The null hypothesis of no association between the known and calculated fractions is rejected at the $P<0.001$ level ($r > 0.96$).

Figure SM3. PC2 scores derived from (a) some major and minor elements and (b) bulk minerals of cores 02PC and 05JPC, as well as the circum-Arctic source areas (Table S1). (c) Box-plot of the log ratio I+K/C showing the relative composition of the sediment from cores 05JPC and 02PC, in comparison with some circum-Arctic sources (Beaufort Sea, Mackenzie Delta and CAA: Gamboa 2017, Chukchi Sea: Khim 2003, Bering Strait: Kalinenko 2001, Eastern Siberian Sea: Khim 2003; Viscosi-Shirley et al. 2003a).

Table SM1. Conventional ^{14}C ages (half-life 5568 years) calibrated with Marine13 (Reimer et al., 2013) using Calib software (v7.1; http:// calib .org /calib/) for core 18TC, 750PC, 56PC and 02PC for three different marine reservoir ages.

1113

1114 **Table SM2**. List of references for the (a) geochemical and (b) mineralogical database used in
1115 this study. SPM = suspended particular matter.

1116

1117 **Table SM3.** Loadings derived from the principal component analysis of the circum-Arctic
1118 geochemical and mineralogical data, illustrating the weight of each (a) element and (b) mineral in
1119 the definition of each PC score. In figure 2, we used the PC2 score instead PC1 because this latter
1120 is influenced by grain size distribution. Thus, PC2 was better representing the geochemical and
1121 mineralogical composition of the surrounding Arctic areas.

1122
1123

1124

Figure 1.

Figure 1
2 column fitting image
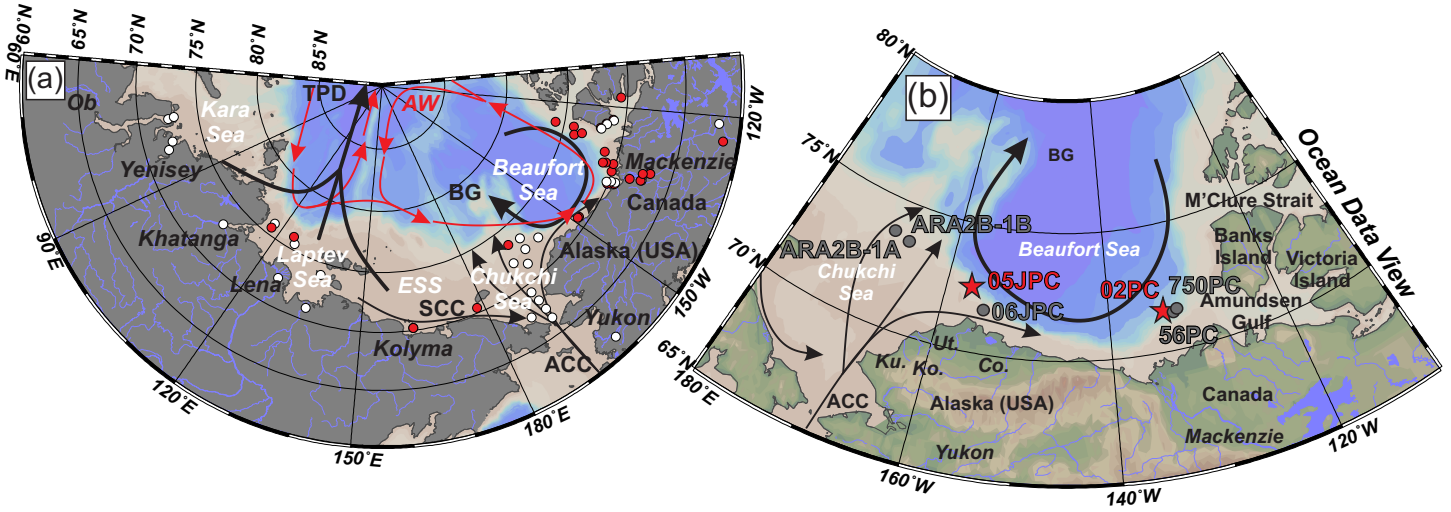
Figure 2.

Figure 2
two column fitting
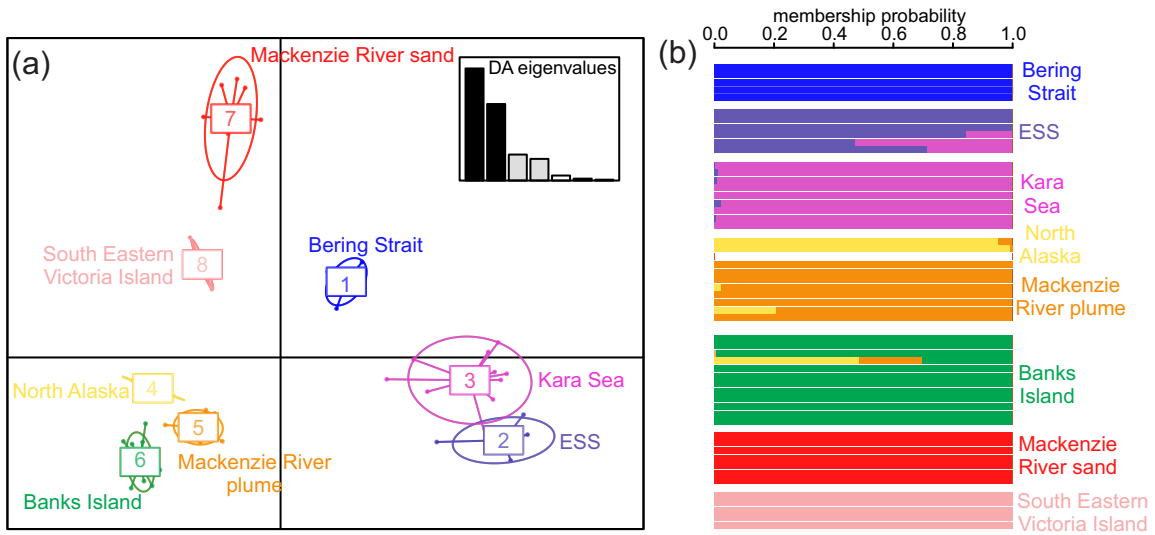
Figure 3.

Figure 3
two column fitting

(a)

02PC
EM1   EM2   EM3

EM1 = 2 µm
EM2 = 6.5 µm
EM3 = 14 µm

loading (Vol %)

Grain size (µm)

05JPC
EM1   EM2   EM3

EM1 = 2 µm
EM2 = 6.5 µm
EM3 = 14 µm

loading (Vol %)

Grain size (µm)

(b)

02PC
EM scores (%)

02PC
CT-scan

IRD1A
IRD2A
IRD2B

Depth (cm)

Age (ka cal BP)

Mean grain size (µm)

05JPC
EM scores (%)

05JPC
Lithology

unit I
unit II
IRD1A
IRD1B

Depth (cm)

Age (ka cal BP)

Mean grain size (µm)

EM1   EM2   EM3
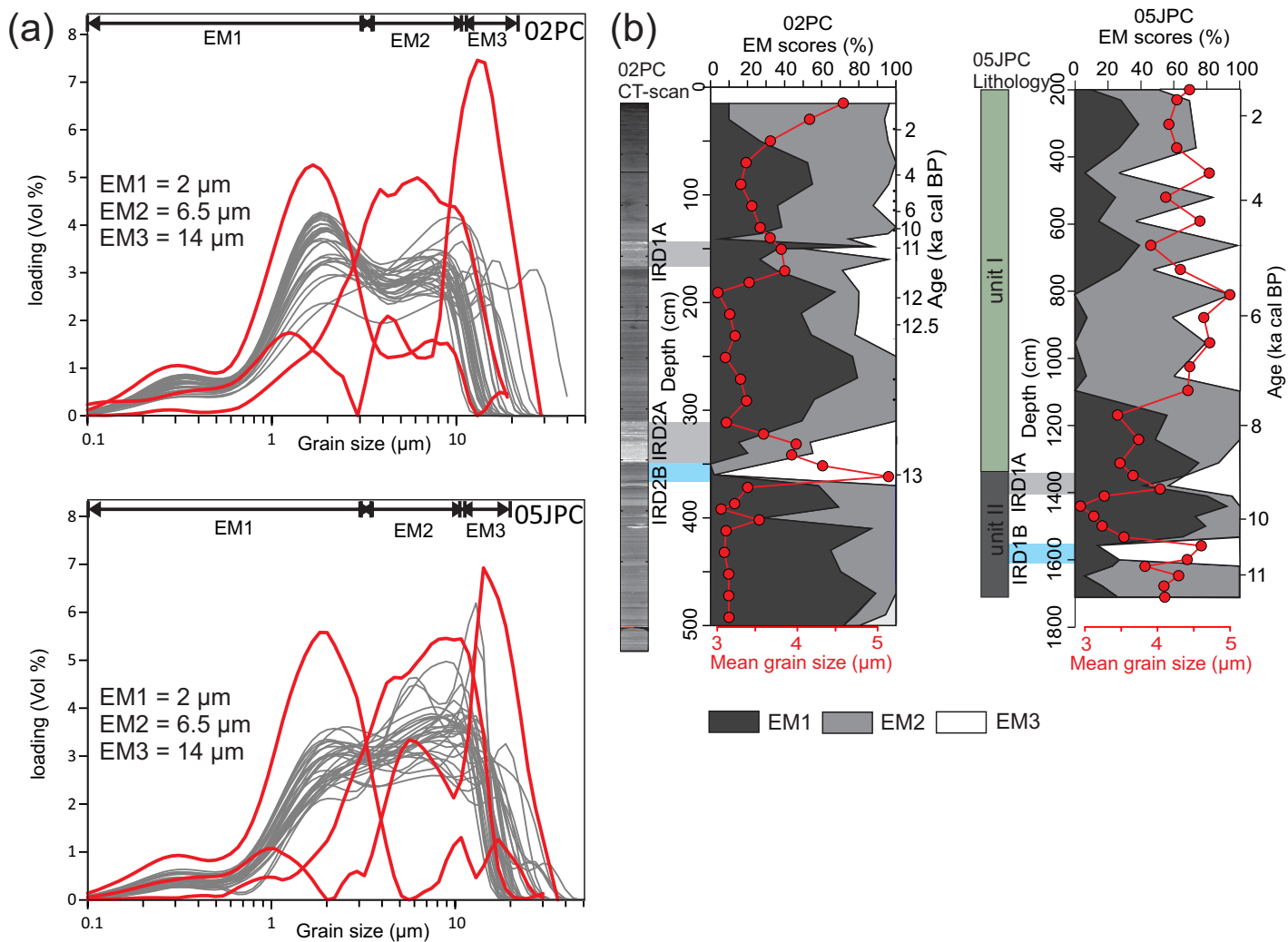
Figure 4.

Figure 4
two column fitting
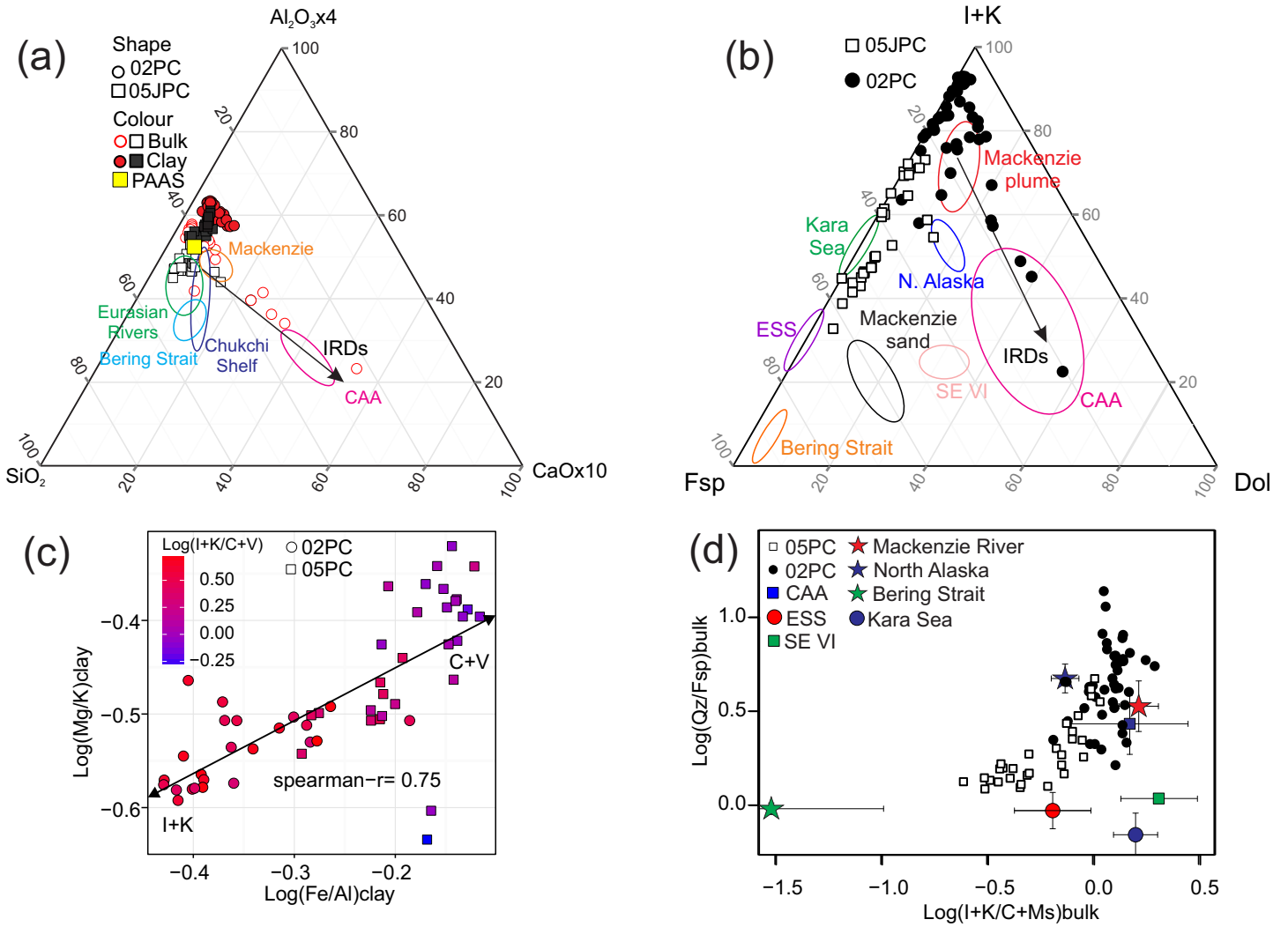
Figure 5.

Figure 5
single column fitting
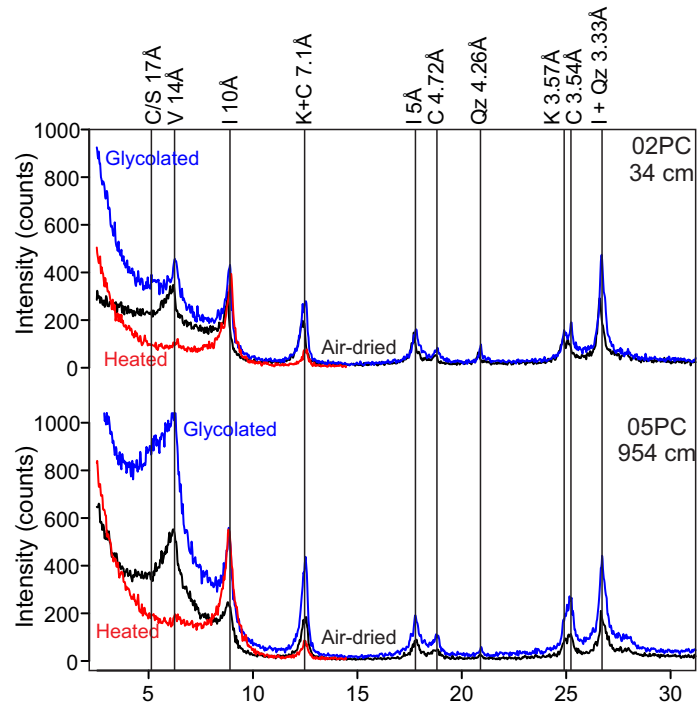
Figure 6.

Figure 6
two column fitting
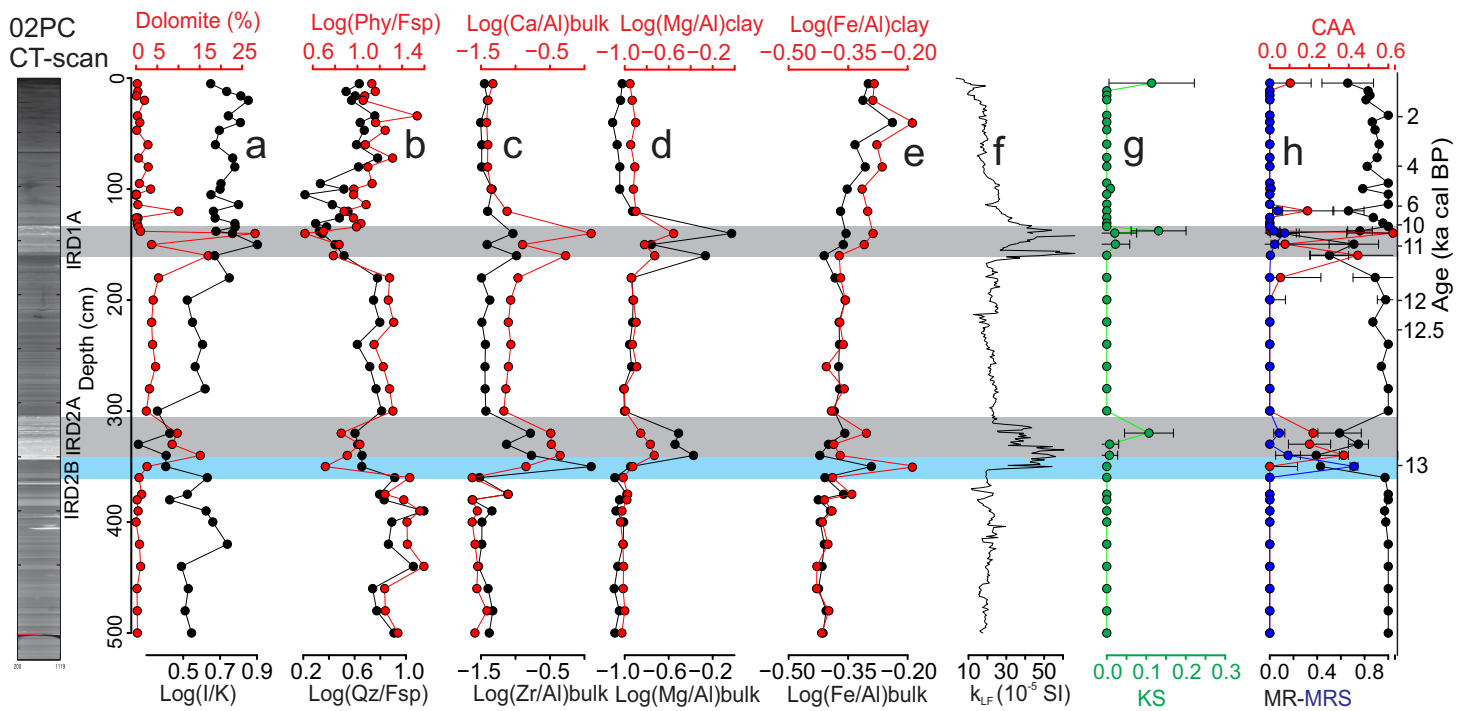
Figure 7.

Figure 7
two column fitting
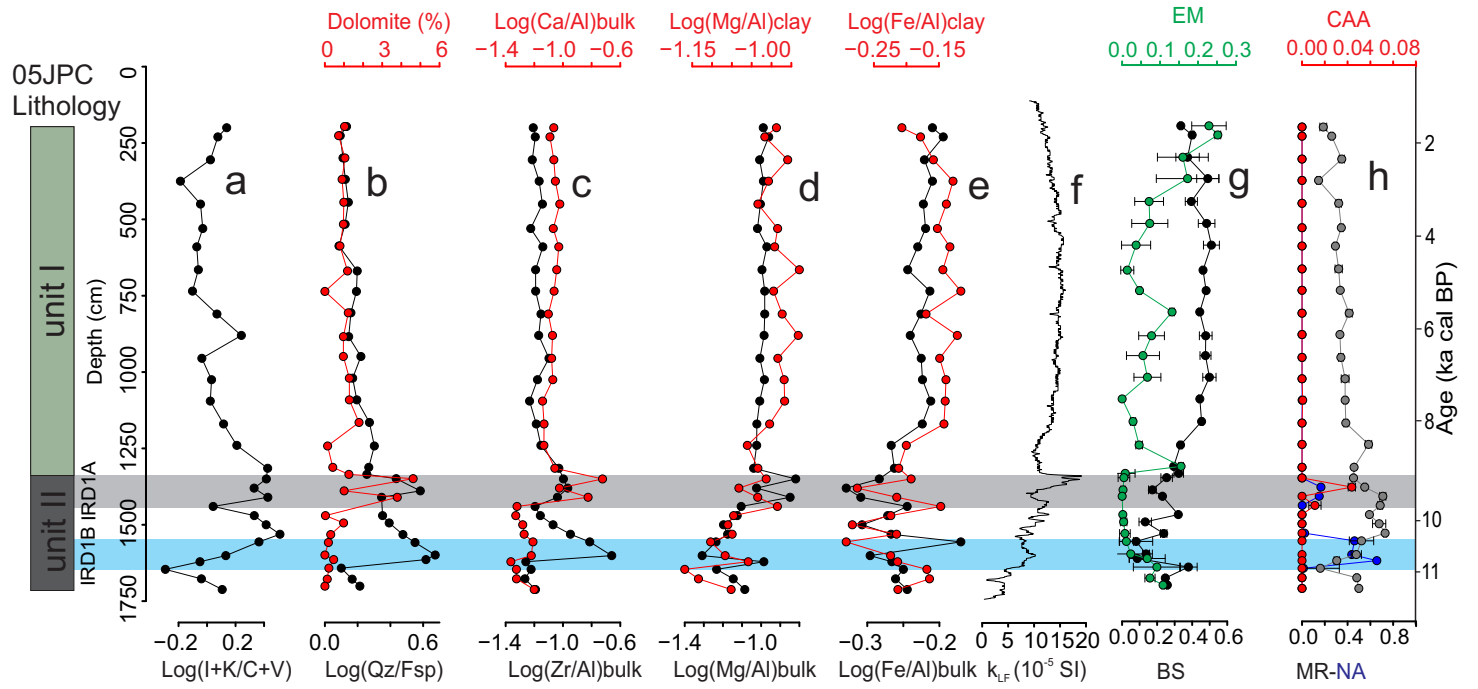
Figure 8.

Figure 8
single column fitting

(a)

Phyllosilicates

- North Rivers:
  -Peel
  -Red

- South Rivers:
  -Tsiigehtchic
  -Fort Simpson
  -Liard
  -Hay
  -Peace
  -Slave

North

South

Plagioclase

K-feldspar

(b)

Age (ka cal BP)

Holocene

MWP-1B

Lake Agassiz

GISP2 δ¹⁸O

YD

RSL (m)

Beaufort Sea

gobal

Anchor Ice-IRD

Log(EM3/EM2)

Log(EM1/EM2)

Mackenzie discharge

CAA

Dolomite (%)

Log(Qz/Fsd)

Log(Phy/Fsd)

Log(I/K)
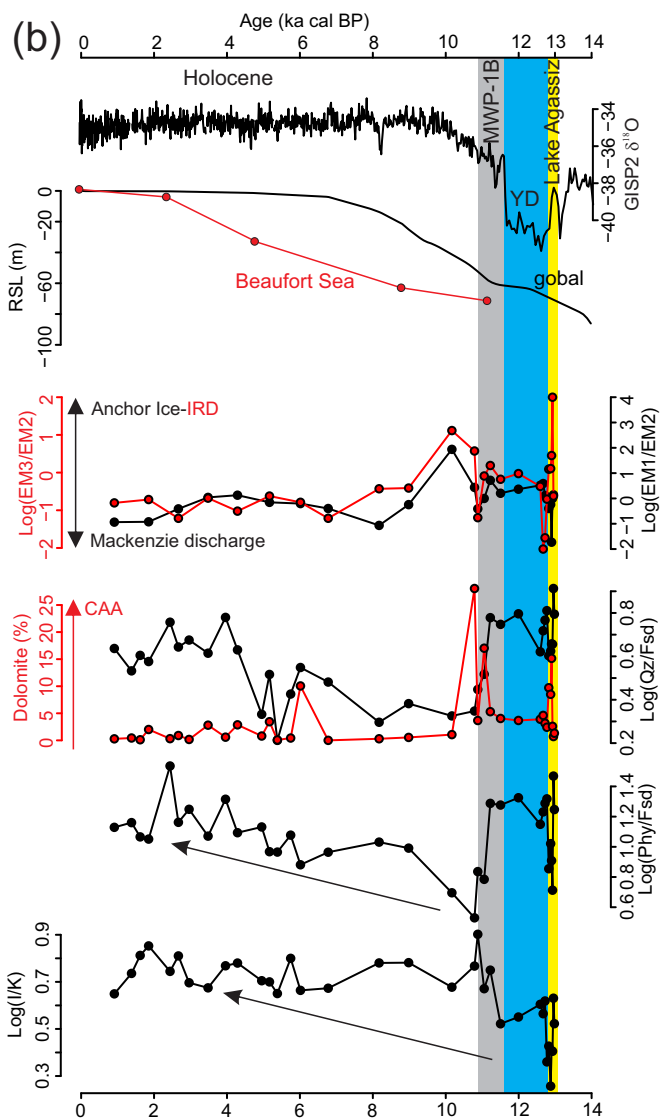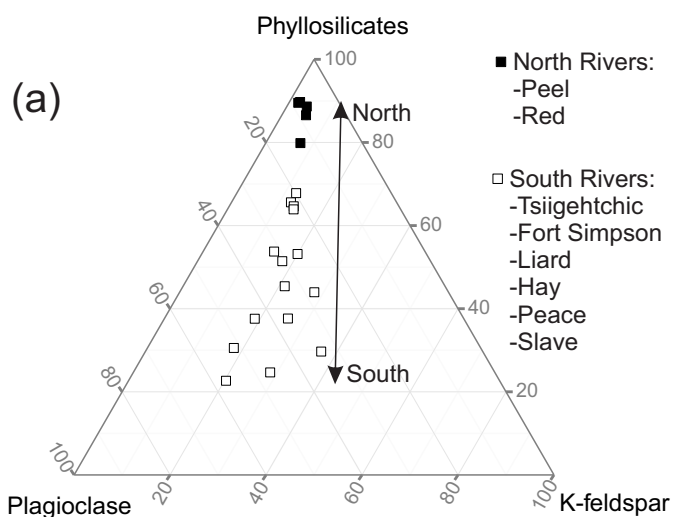
Figure 9.

Figure 9
single column fitting
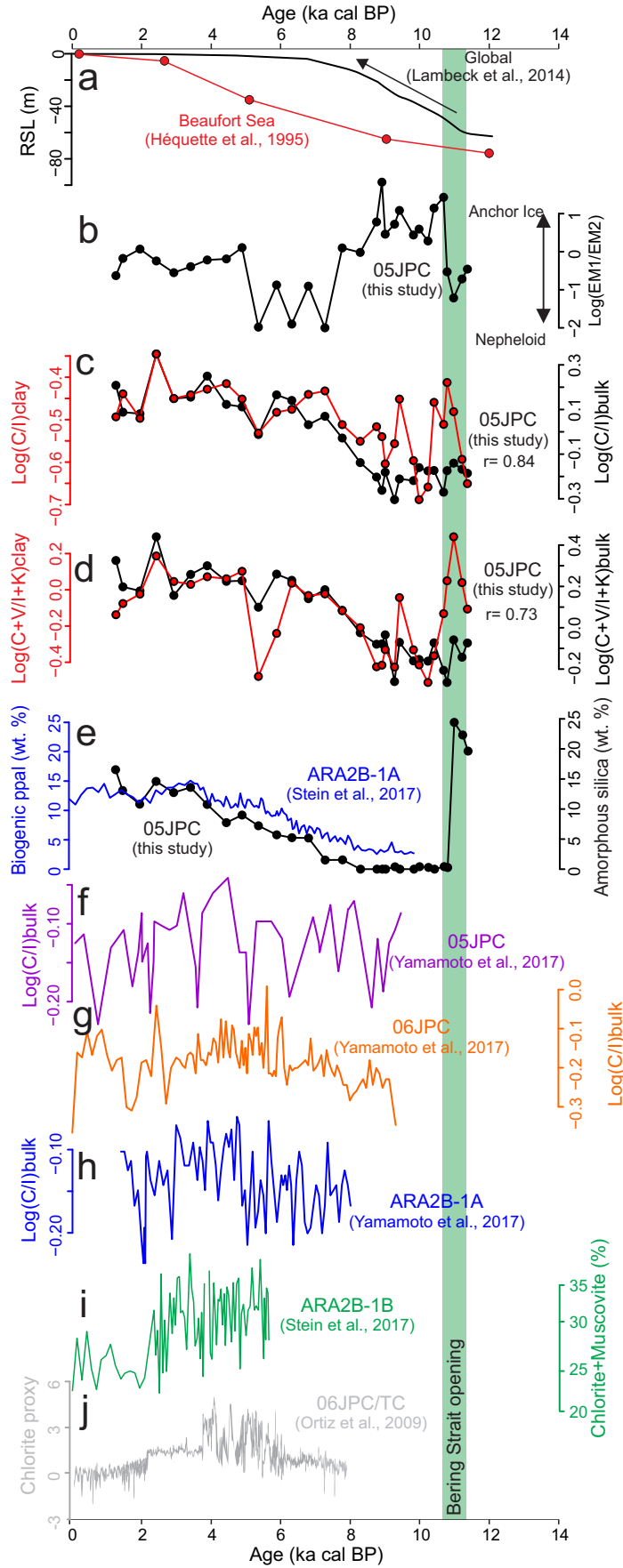
Figure 10.

Figure 10
single column fitting